Title

Mechanisms of amphibian arrestin 1 self-association and dynamic distribution in retinal photoreceptors.

Journal

Journal of Biological Chemistry, 300(12)

Authors

Barnes, Cassandra
Salom, David
Namitz, Kevin
et al.

Publication Date

2024-11-05

DOI

10.1016/j.jbc.2024.107966

Peer reviewed

JBC RESEARCH ARTICLE

Mechanisms of amphibian arrestin 1 self-association and dynamic distribution in retinal photoreceptors

Received for publication, July 8, 2024, and in revised form, October 15, 2024 Published, Papers in Press, November 5, 2024,
https://doi.org/10.1016/j.jbc.2024.107966

Cassandra L. Barnes[1,‡], David Salom[2,‡], Kevin E. W. Namitz[3], W. Clay Smith[4], Bruce A. Knutson[3], Michael S. Cosgrove[3], Philip D. Kiser[2,5,6,*], and Peter D. Calvert[1,*]

From the [1]Center for Vision Research and the Department of Ophthalmology and Visual Sciences, SUNY Upstate Medical University, Syracuse, New York, USA; [2]Department of Ophthalmology, Gavin Herbert Eye Institute – Center for Translational Vision Research, University of California, Irvine, California, USA; [3]Department of Biochemistry and Molecular Biology, SUNY Upstate Medical University, Syracuse, New York, USA; [4]Department of Ophthalmology, University of Florida, Gainesville, Florida, USA; [5]Department of Physiology & Biophysics, University of California, Irvine, California, USA; [6]Research Service, VA Long Beach Medical Center, Long Beach, California, USA.

Reviewed by members of the JBC Editorial Board. Edited by Kirill Martemyanov

Visual arrestin 1 (Arr1) is an essential protein for termination of the light response in photoreceptors. While mammalian Arr1s form dimers and tetramers at physiological concentrations *in vitro*, oligomerization in other vertebrates has not been studied. Here we examine self-association of Arr1 from two amphibian species, *Xenopus laevis* (xArr1) and *Ambystoma tigrinum* (salArr1). Sedimentation velocity analytical ultracentrifugation showed that xArr1 and salArr1 oligomerization is limited to dimers. The K_D for dimer formation was 53 μM for xArr1 and 44 μM for salArr1, similar to the 69 μM K_D for bovine Arr1 (bArr1) dimers. Mutations of orthologous amino acids important for mammalian Arr1 oligomerization had no impact on xArr1 dimerization. Crystallography showed that the fold of xArr1 closely resembles that of bArr1 and crystal structures in different space groups revealed two potential xArr1 dimer forms: a symmetric dimer with a C-domain interface (CC dimer), resembling the bArr1 solution dimer, and an asymmetric dimer with an N-domain/C-domain interface. Mutagenesis of residues predicted to interact in either of these two dimer forms yielded modest reduction in dimer affinity, suggesting that the dimer interfaces compete or are not unique. Indeed, small-angle X-ray scattering and protein painting data were consistent with a symmetric anti-parallel solution dimer (AP dimer) distinct from the assemblies observed by crystallography. Finally, a computational model evaluating xArr1 binding to compartment-specific partners and partitioning based on heterogeneity of available cytoplasmic spaces shows that Arr1 distribution in dark-adapted photoreceptors is largely explained by the excluded volume effect together with tuning by oligomerization.

Arrestins are a family of proteins that play important roles in intracellular signaling by G protein coupled receptors (GPCRs) (reviewed in (1)). They are ubiquitous—each cell in the body expressing at least one of the four family members consisting of two visual arrestins, Arr1 and Arr4, and two nonvisual arrestins, Arr2 and Arr3, that have similar structures and share ∼50% sequence identity. The nonvisual arrestins, first identified as modulators of β-adrenergic receptors, are also known as β-arrestin-1 and -2. All arrestins are involved in terminating GPCR signaling by binding to activated receptors and sterically blocking G protein activation. β arrestins have additional roles, including desensitization of signaling cascades by removing GPCRs from the plasma membrane. The main function of visual arrestins is to halt phototransduction in photoreceptor cells by binding to light-activated, phosphorylated opsins, the GPCRs responsible for sensing photons (2–7).

Common to all mammalian arrestins, except cone arrestin (Arr4) (8), is the propensity to form oligomers at physiological concentrations *in vitro* (8–13). Oligomerization of β-arrestin-2 was recently shown to be important for activating signaling pathways through receptor independent mechanisms (14). Arr1 oligomers serve as a storage form of Arr1 since only monomers bind phosphorylated light-activated rhodopsin (P-Rh*) (15, 16). The binding of Arr1 to P-Rh* shuts off the activation of the G protein, transducin, and thus begins the termination of the photoresponse. Because the kinetics of the photoresponse are critical for vision, the timing of photoresponse termination is of utmost importance and Arr1 oligomerization is thought to set the monomer concentration at the appropriate level for this task. Related to this, Arr1 oligomerization is thought to drive its light-dependent subcellular distribution through mechanisms that include its partitioning into the photoreceptor inner segment (cell body) by a steric volume exclusion mechanism (17) and/or amplifying the impact of low abundance, low affinity non-rhodopsin binding partners (18–20) in dark-adapted rods dramatically reduces the Arr1 content in the photoreceptor outer segment—the rod organelle where phototransduction takes place (17, 19). Thus, arrestin oligomerization plays major roles in controlling cell signaling, making understanding the mechanisms underlying this phenomenon essential from a functional and therapeutic perspective.

‡ These authors contributed equally to this work.
* For correspondence: Philip D. Kiser, pkiser@uci.edu; Peter D. Calvert, calvertp@upstate.edu.

The mechanisms of arrestin oligomerization in mammalian Arr1-3 are diverse, employing different interaction domains where electrostatic and hydrophobic interactions are at play (21). A notable feature of mammalian Arr1 is that it undergoes dimerization followed by tetramerization, with no trimer intermediate (12, 22). Molecular modeling and EPR spectroscopy of mammalian Arr1 suggests that dimers form through interactions of two C-termini and tetramers form from the subsequent interactions of four N-termini (16, 23). Although light-dependent redistribution of Arr1 has been well documented in the African clawed frog, *Xenopus laevis* (24, 25), it is not known whether or how Arr1 of nonmammalian vertebrates form oligomers.

Here we examined the oligomerization of arrestin-1 from the African clawed frog, *X. laevis*, (xArr1) and the tiger salamander, *Ambystoma tigrinum* (salArr1), popular model organisms for cell biology and biophysical studies. We show that xArr1 and salArr1 formed dimers, but not tetramers, at physiological concentrations. Crystal structures obtained at 2.5 to 2.9 Å-resolution and mutagenesis studies of predicted oligomer interaction sites show that xArr1 may form dimers through a predicted CC interface that, although similar to that predicted for the solution structure of bArr1 (23), involves distinct residues at the contact surface. Unlike mammalian arrestin 1, a second crystal-predicted CN dimer appears to compete with the CC dimer. Comparison of the CC dimer crystal structure suggests that the lack of xArr1 tetramer formation is due to rotation of the N-domains to a position that is unfavorable for efficient interaction with a second CC dimer. However, small angle X-ray scattering (SAXS) data indicates that a distinct, anti-parallel dimeric structure (AP dimer) involving contacts between the C-edge and middle loop forms in solution. The solution dimer does not appear to involve the interaction surfaces predicted from the crystal structures. Protein painting-mass spectrometry results support the anti-parallel dimer model. These data indicate that the xArr1 dimer could be a mixture of structurally distinct assemblies. Using a computational model, we show that, despite the lack of tetramer formation, the vast majority of the cell body–biased distribution of Arr1 in dark-adapted photoreceptors can be explained by size-dependent cytoplasmic partitioning driven by the steric volume exclusion effect (17). Indeed, even if Arr1 exists solely as monomer *in vivo*, partitioning by steric volume exclusion is predicted to account for most of its cell-body enrichment. The model predicts that association with low-affinity binding partners within the cell body would require binding partner concentrations exceeding that of rhodopsin in the outer segment to have substantial impact on inner segment localization, making such a mechanism unlikely.

Results

Primary structure of X. laevis *Arr1 diverges from mammalian Arr1*

Analysis of published amino acid sequences (Fig. 1) shows *X. laevis* Arr1 (xArr1) and *A. tigrinum* Arr1 (salArr1) are 75% identical. xArr1 and salArr1 have 65% and 67% sequence identity, respectively, and ∼85% sequence similarity to bArr1. xArr1 is eight residues shorter than bArr1. Bovine, mouse, and human Arr1 are greater than 80% identical, thus showing sequence divergence between mammalian and amphibian proteins. Residues that constitute the polar core, a series of buried charged residues that interact electrostatically and act as a phosphosensor in mammalian arrestins (10, 26, 27), are completely conserved (Fig. 1, red arrowheads). Three cysteine residues that are important for the stability of the protein (28) are conserved as well (Fig. 1, black arrowheads). In bArr1, residues F85 and F197 (Fig. 1, brown arrowheads) reside at the dimer and tetramer interfaces (23), and these two sites are strictly conserved among mammalian Arr1s. Alanine mutations at these positions disrupt tetramer formation at physiological concentrations and increase the dimer dissociation constant (K_D) tenfold (22) in mammalian Arr1s. In xArr1, these two sites contain Tyr (Y84) and Phe (F193) residues, demonstrating their moderate to strong conservation outside of the group of mammals. The highest areas of sequence divergence between xArr1 and the mammalian proteins reside mostly in areas expected to be at the molecular surface, including residues at the beginning of the N terminus (xArr1 1–11; bArr1 1–12), a stretch spanning β-strand VI and helix I in the N-domain (xArr1 84–101; bArr1 85–102), the 160-loop (xArr1 152–156, bArr1 153–160), and the acidic C-tail (xArr1 355–359, 364–369, 377–396; bArr1 359–365, 370–375, 383–404). Significant differences to note in these spans are two *Xenopus* residues M11 and M369, which are homologous to I12 and F375 in bArr1. In bArr1, these residues participate in a hydrophobic network present in beta-strand I, helix I, and beta-strand XX, known as the three-element interaction, which is important for stabilizing the basal conformation of arrestin and maintaining specificity for phosphorylated receptor (26, 29).

Amphibian Arrestin1 dimerizes in a concentration-dependent manner, but does not form tetramers

Initial crystallography studies of bArr1 suggested that the protein formed a tetrameric assembly as observed in the crystallographic asymmetric unit (26, 30). Studies using multi-angle light scattering (MALS), AUC sedimentation velocity, small-angle x-ray scattering, and double electron-electron resonance spectroscopy (DEER) also showed mammalian Arr1 dimeric, and in some studies tetrameric, self-association (10–12, 16, 22, 23). To investigate whether amphibian Arr1 has similar propensity to self-associate, we subjected samples of purified recombinant xArr1 or salArr1 to sedimentation velocity analytical ultracentrifugation at concentrations ranging from 5 μM to 308 μM (Fig. 2, *A* and *B*). Sedimentation profiles were analyzed with SEDFIT using a continuous c(s) distribution model (31). The lowest concentrations of both Arr1 proteins yielded a single monomeric peak at a Svedberg (S) value of ∼2.5 S. At higher concentrations, two peaks were detected, one between 2.4 and 2.6 S and another between 2.9 and 3.1 S, which correspond to the monomer and dimer, respectively. The protein mass shifted between the two peaks

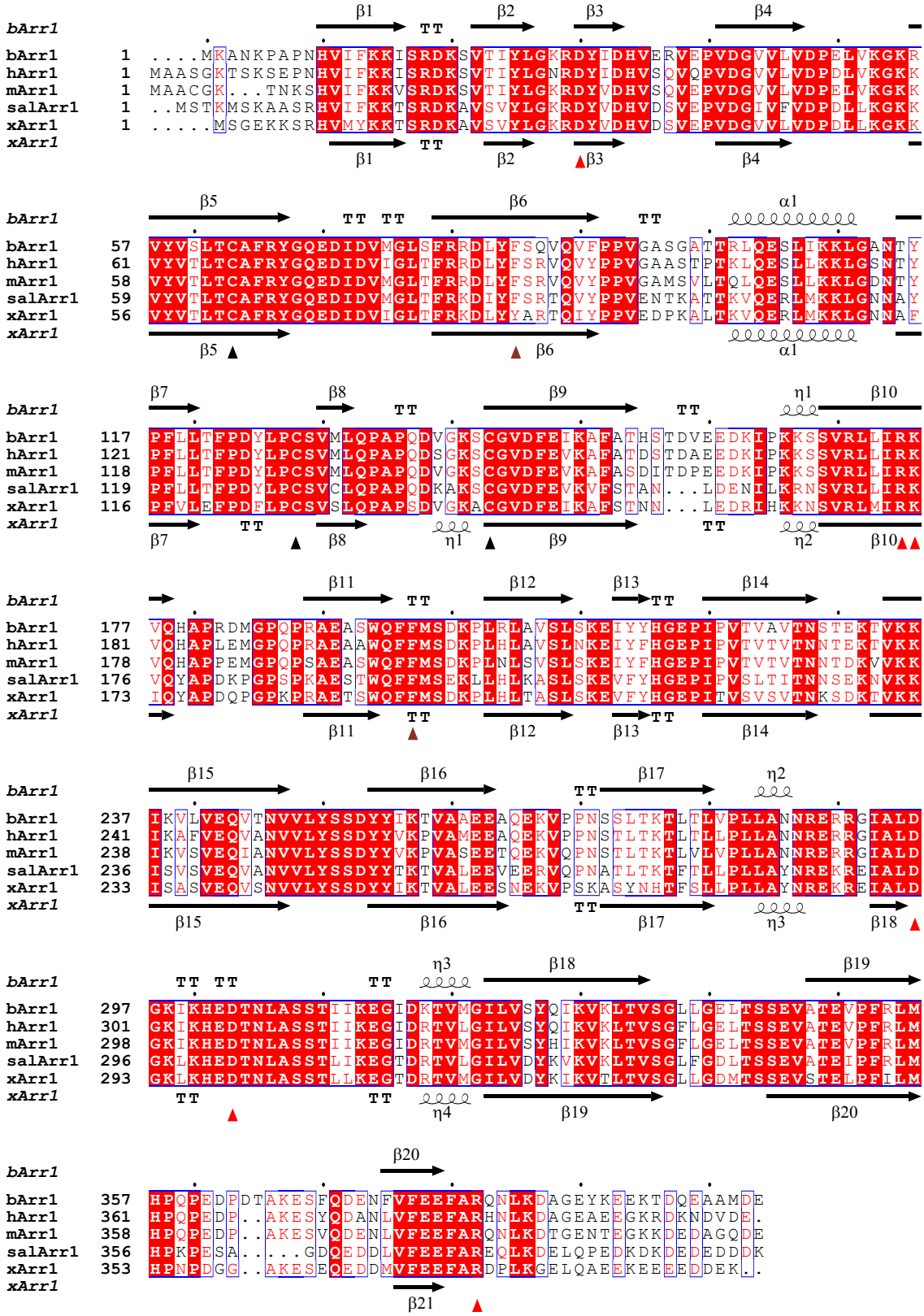

Figure 1. Comparison of *Xenopus laevis* and *Ambystoma tigrinum* Arr1 with mammalian Arr1 sequences. Sequence alignment of *X. laevis* and *A. tigrinum* Arr1 (xArr1 and salArr1, respectively) with bovine (b), mouse (m), and human (h) Arr1s. The alignment was performed with Clustal Omega (88). *White* letters on *red* background indicates exact conservation at a site and boxed *red* letters show partial conservation at a site. Conservation was assigned based on % equivalence of physicochemical properties using a global score of 0.7, as defined in Espript (89). *Red* arrowheads mark residues that form the polar core, *brown* arrowheads mark sites involved in the bArr1 dimer interface, and *black* arrowheads mark conserved cysteine residues. Secondary structural elements derived from crystal structures are shown above and below the sequence alignment. β – beta sheet, α – alpha helix, η – 3_{10} helix.

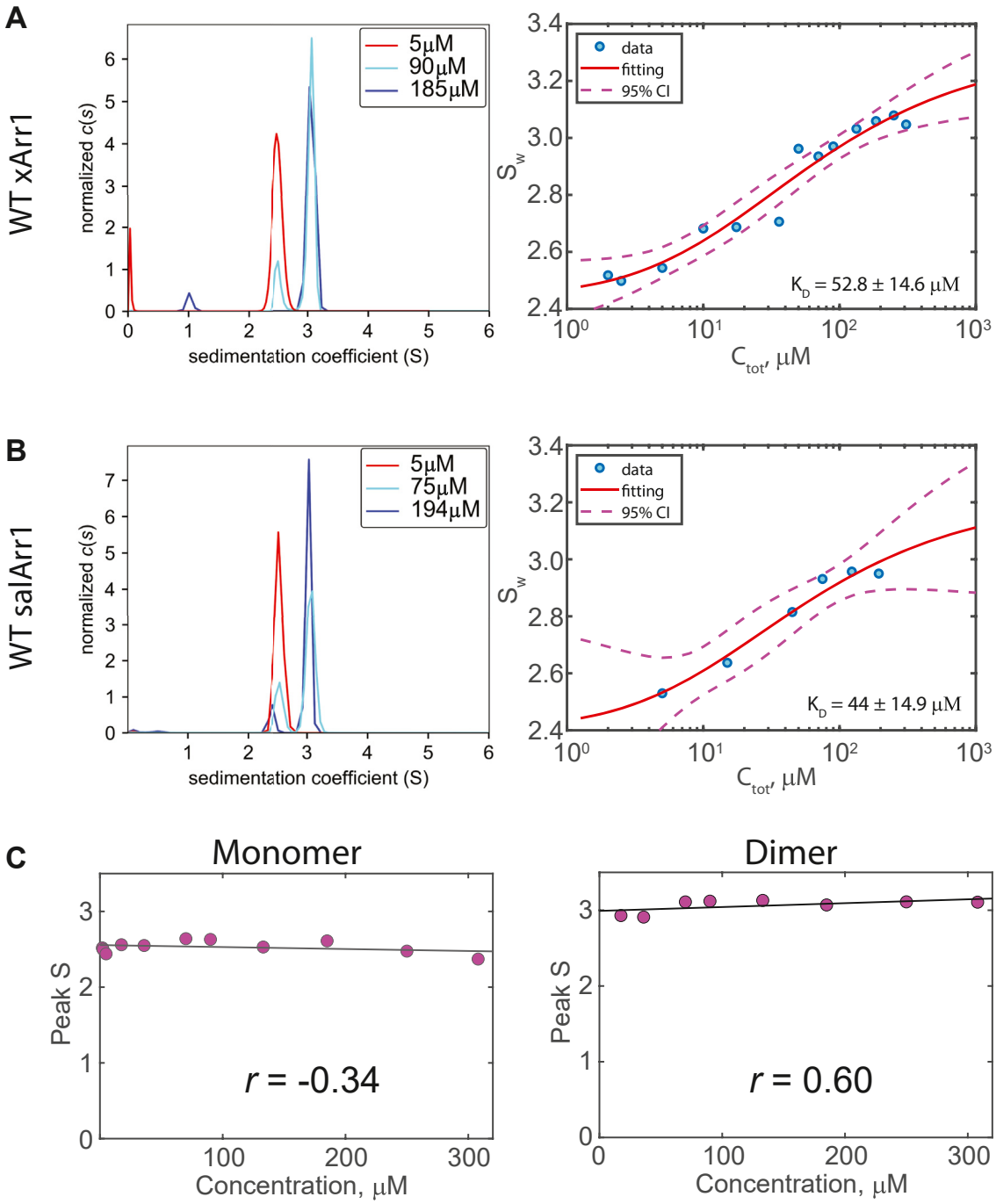

Figure 2. WT Xenopus and Salamander Arr1 form dimers, but not higher-order oligomers, in a concentration-dependent manner. *A*, c(s) distributions for xArr1 at concentrations of 5, 90, and 185 μM (*left* panel) show two peaks at ∼ 2.5 and ∼3 S, consistent with expectations for monomer and dimer. The mass in the peaks shifted from 2.5 S to 3 S with increasing concentration, indicating concentration-dependent self-association to dimers. *Right* panel: symbols are weighted-average S values plotted as a function of concentration. Solid *red* line is the best fitting of the results to the MD model, where monomer and dimer S values were constrained by the average peak positions found in panel *C*, yielding K_D = 52.8 ± 14.6 μM. *Dashed red* lines indicate the 95% confidence interval boundaries of the fitting. *B*, c(s) distributions for salArr1 at concentrations of 5, 75, and 194 μM (*left* panel) show similar peaks at ∼ 2.5 and ∼ 3 S, with similar concentration-dependent shift in mass from 2.5 to 3 S. *Right* panel: symbols and lines as in (A), where MD model fitting yielded K_D = 44.0 ± 14.9 μM. *C*, peak S values (symbols) for the putative monomers and dimers of xArr1 plotted as a function of concentration. Lines represent linear regressions where the slopes were near zero. Mean peak values: 2.53 ± 0.08 and 3.06 ± 0.08 (mean ± SD). *r* represents the Pearson correlation coefficient.

in a concentration-dependent manner, being found solely in the ∼2.5 S peak at 2 to 5 μM and solely in the ∼3.0 S peak at ≥185 μM. While there were small variations in S values for the monomer and dimer xArr1 peaks, there was no systematic increase in the Svedberg coefficients as a function of concentration (Fig. 2*C*), indicating that formation of oligomers larger than dimers is unlikely at physiological concentrations and that the interaction occurs under the slow kinetic regime

relative to the timescale of sedimentation, meaning the k_{off} values are $\sim 1 \times 10^{-5}$ s^{-1} or slower (32). The fact that the SalArr1 had essentially identical behavior to xArr1 suggests that limitation to dimers is a general feature of amphibian Arr1s, We next plotted the S values, weighted by the integral of the c(s) peaks (S_w), as a function of Arr1 concentration and fitted them with a dimerization isotherm to determine the monomer-dimer binding affinity (Fig. 2, *A* and *B*,right panels). The $K_{D,dimer}$ for xArr1 was found to be 52.8 ± 14.6 μM (mean ± SEM) and that of salArr1 was found to be 44.0 ± 14.9 μM, values that fall between the previously reported $K_{D,dimer}$ for bovine (37 μM) and mouse (57.5 μM) Arr1 (22) (Table 1), although, as shown below, we find a somewhat different $K_{D,dimer}$ value for bArr1.

Bovine visual arrestin forms higher order oligomers

Previous studies characterizing the oligomerization of bArr1 have reached variable conclusions. Some reported dimer formation only (9, 11, 33) and others reported both dimer and tetramer formation (10, 12, 16, 23). Thus, it is not clear if our observed dimer-limited oligomerization of xArr1 represents the universal mode of Arr1 oligomerization. To directly compare our results for xArr1 to those of bArr1, we examined the concentration-dependent oligomerization of bArr1 under identical conditions (Fig. 3). Both recombinant bArr1 and endogenous bArr1 purified from bovine rod outer segment preparations were used to examine the impact of different protein sources on oligomerization behavior. AUC sedimentation velocity experiments were performed over a range of 5 to 220 μM bArr1 (Fig. 3*A*). Three distinct species are observed in a concentration-dependent manner. At the lowest concentration of 5 μM, a single peak was observed at ∼2.5 S (Fig. 3*A*). At 15 μM, two peaks were observed at ∼2.5 and ∼3 S, corresponding to the monomer and dimer, respectively. At higher concentrations, two peaks continued to be observed that shifted to higher s-values with higher concentrations. The absence of a third peak in the *c*(s) plots that would represent monomer, dimer, and tetramer species suggests that dimers and tetramers form under the rapid kinetic regime relative to the timescale of sedimentation, with k_{off} values ≥ 1×10^{-4} s^{-1} (32). Under this regime, the peak at lower S likely represents the average S value of a mixture of monomer and dimer species that cannot be resolved within the signal-to-noise of the experiment, while the peak at higher S likely represents a mixture of dimer and tetramer. These results are consistent with prior reports that bovine Arr1 self-associates up to tetramers. To emphasize the difference in the behavior of xArr1 and bArr1, overlay plots of two concentrations of each protein that span the range of oligomerization are shown in Fig. 3*B*. Note that the position of monomer xArr1 and bArr1 are not necessarily expected to overlie since small differences in the shapes of the proteins may lead to slightly different S values. Moreover, even the lowest concentration of bArr1 examined (5 μM) may be a mixture of monomer with a small amount of dimer, which leads to broadening of the peak.

S_w isotherm analysis was best fitted with a monomer-dimer-tetramer model yielding a K_D^D of 69.0 ± 35.2 μM for the monomer-dimer equilibrium and a K_D^T of 25.1 ± 5.5 μM for the dimer-tetramer formation (mean ± SE, Fig. 3*C*). These values are slightly higher than those published previously (10, 22) but agree with the reported cooperativity of tetramer formation found for bArr1 (12, 22). The larger errors about the K_D^D and K_D^T, 51% and 22%, respectively, largely reflect uncertainty in the Svedberg constants for the dimer and tetramer forms of bArr1, neither of which were resolved owing to fast binding and unbinding during the AUC run, thus making the fitting difficult to constrain.

Mutations that eliminate tetramerization and reduce dimerization in mammalian Arr1 slightly increase xArr1 dimerization affinity

The first crystal structures of bovine Arr1 showed the asymmetric unit to be a tetramer with contacts at NN, NC, and CC domain interfaces (26, 30). However, a later study investigating mutations predicted to disrupt Arr1 self-association revealed that the crystal tetramer may not be the physiologically relevant structure (16). Further investigations led to a solution structure model where the dimer forms predominantly at the CC interface, followed by NN interactions to form the tetramer (23). It was reported that the mutation of two phenylalanine residues predicted to be at the NN and CC interfaces of mouse and bovine Arr1 protomers in the solution

Table 1
Dissociation constants for Arr1 proteins

Protein	$K_{D\ dimer}$ (μM)		$K_{D\ tetramer}$ (μM)
Bovine Arr1	69.0 ± 35.2		25.1 ± 5.5
Mouse Arr1	57.5 ± 0.6		63.1 ± 2.6
Human Arr1	2.95 ± 0.02		224 ± 5
Xenopus Arr1	52.8 ± 14.6		–
Tiger Salamander Arr1	44 ± 14.9	(NS)	–
xArr1-Y84A	16.4 ± 8.2	(NS)	–
xArr1-F193A	23.5 ± 14.1	(NS)	–
xArr1-Y84A;F193A	20.6 ± 13.8	(NS)	–
xArr1-T188A;Q191A	183 ± 57	([a])	–
xArr1-P182A-R185A;T188A-Q191A	74 ± 43	(NS)	–
xArr1-S136A;D137A	20.2 ± 11.2	(NS)	–
xArr1-L156A;E157A;T188A-Q191A;D337A;S340A	4.03 ± 1.11	([a])	–

All values are from this study except for mouse and human Arr1, which are from (22). Values are K_D ± standard error obtained from curve fitting. (NS), K_D is not significantly different from that of *Xenopus* Arrestin 1.
[a] K_D is significantly different from that of *Xenopus* Arrestin 1, $p < 0.05$.

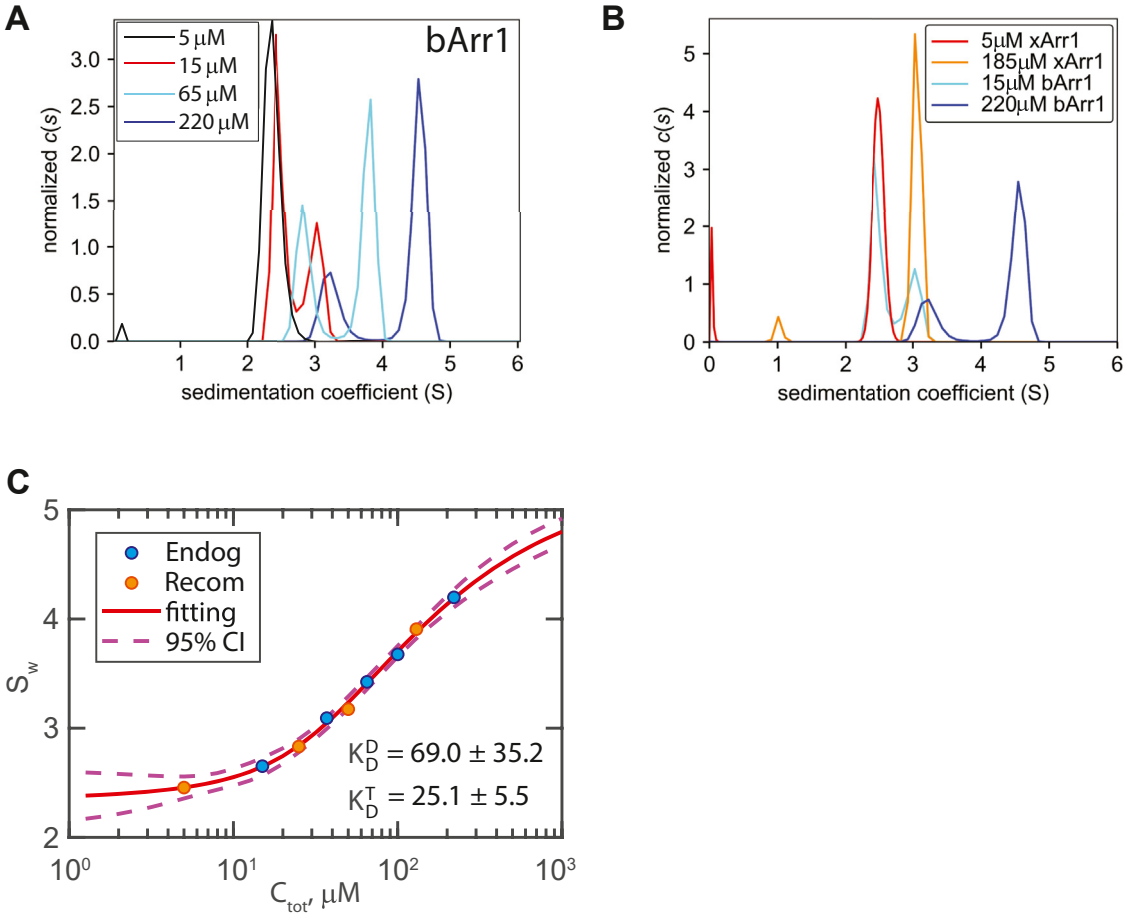

Figure 3. WT bovine Arr1 forms larger oligomers. *A*, c(s) distributions for bArr1 show two peaks that shift to higher S values with increasing concentration. *B*, overlay of two concentrations each of xArr1 and bArr1 showing that the monomer and dimer of both species sediment at similar Svedberg values at lower concentrations. The Svedberg value of the right-most peak of bArr1 (220 μM) is approximately consistent with that expected for a globular protein with molecular weight of an Arr1 tetramer. *C*, weighted S isotherm analysis. Symbols indicate the weighted average Svedberg values at indicated concentration. *Blue* symbols represent S_w values for endogenous bArr1 purified from bovine rod outer segments. *Orange* symbols represent S_w values for recombinantly expressed bArr1. The *red* line is the best fitting of the MDT binding model to the pooled endogenous and recombinant values, yielding $K_{D,\ dimer} \sim 69$ μM and $K_{D\ tetramer} \sim 25$ μM. *Dashed* lines are 95% confidence interval boundaries.

model to alanine abolished the formation of tetramers and increased the K_D^D approximately 10-fold (22, 23). To determine whether xArr1 uses either of these interfaces to dimerize, we examined the effect of mutating the corresponding xArr1 residues Y84 and F193 to alanine. In contrast to mammalian Arr1s, the alanine mutations, either alone or in combination, appeared to slightly enhanced xArr1 dimer formation (Fig. 4). The apparent K_D^D values of 23.7 ± 8.2 μM, 23.5 ± 14.1 μM, and 20.6 ± 13.8 μM, for Y84A, F193A, and Y84A/F193A, respectively, were less than half the apparent WT xArr1 K_D^D of 52.8 ± 14.6 μM, although these differences did not reach statistical significance under multiple pairwise analysis (Table 1). Together, these results suggest that xArr1 uses a novel interface and/or mechanism to form dimers.

Two crystal structures of xArr1 reveal two potential dimer interfaces

To further explore the structural basis for the xArr1 oligomerization behavior, we solved crystal structures of xArr1 in space groups $P3_121$ ($xArr1_{SG1}$) and $P3_221$ ($xArr1_{SG2}$), each containing a single xArr1 monomer in the asymmetric unit (Fig. 5*A* and Table 2). The two xArr1 crystal forms exhibited similar overall tertiary structure, although some significant differences were found at the C-edge (Fig. 5*A*) and at the region of the 3-element interaction (34) where the C terminus of $xArr1_{SG2}$ was disordered (Fig. 5*B*, left panel). The C-tail region was variably ordered in the two xArr1 structures. In $xArr1_{SG1}$, C-tail residues 368 to 379 are well-resolved and are similar in structure to the corresponding region of bArr1 while the final 17 residues were not observed (Fig. 5*A*). To the contrary, electron density representing the C-tail region was not observed for $xArr1_{SG2}$. In both structures, the finger loop (residues 67–77) is nestled in a positively charged groove formed by the N-domain, which prevents the terminal C-tail region of $xArr1_{SG1}$ from adopting the 'basal' conformation observed for bArr1. The polar core in $xArr1_{SG1}$ (Fig. 5*B*, right panel) is structurally similar to that of basal bArr1 (Fig. 6*A*). However, the polar core is disrupted in $xArr1_{SG2}$, as evident from the absence of the C-tail residue R376 and the movement of R28 towards the polar core (Fig. 5*B*, right panel). There is a small (∼ 4°) interdomain rotation when comparing the two xArr1 structures.

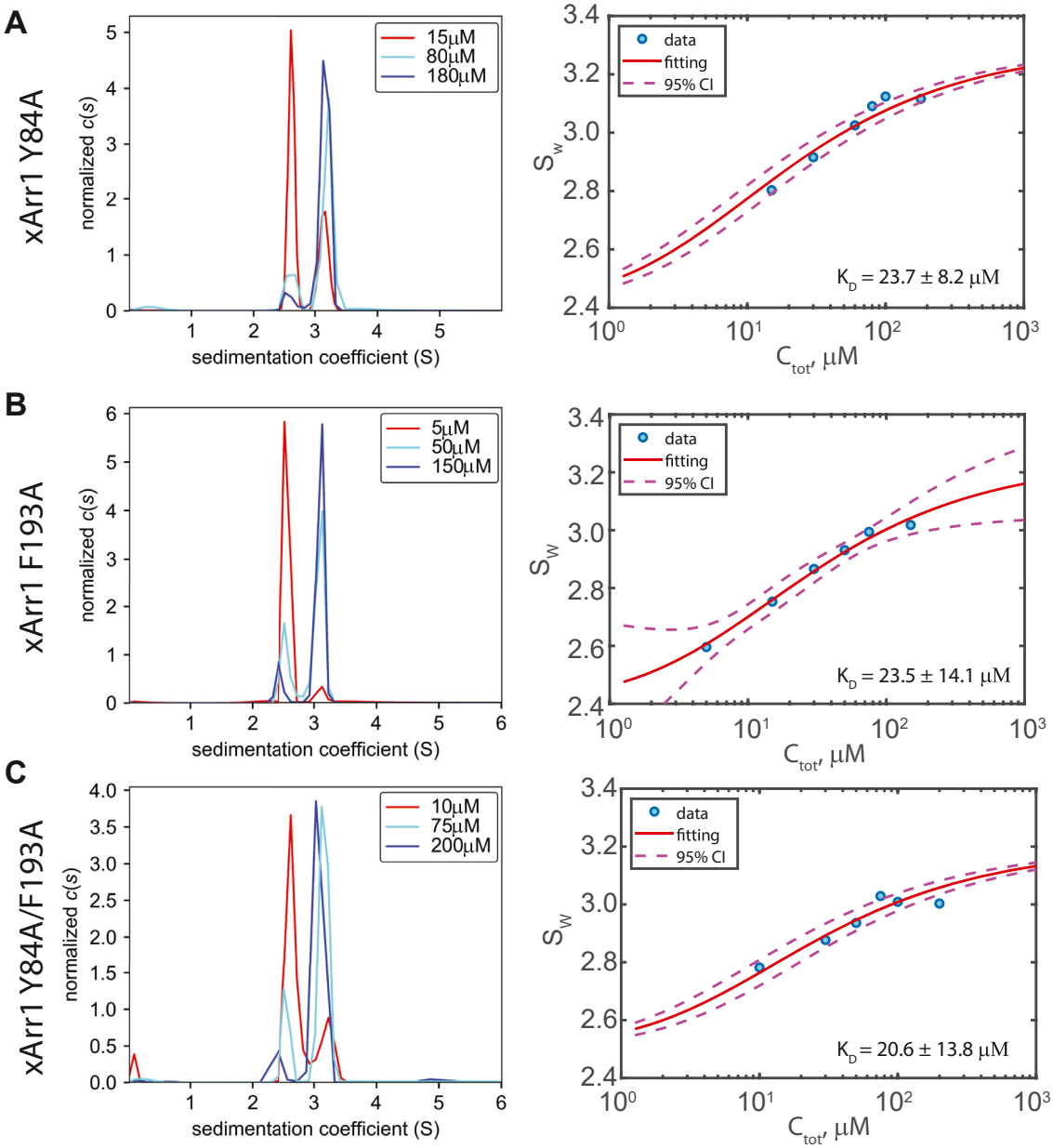

Figure 4. Mutations homologous to those that disrupt mammalian Arr1 oligomerization do not impact xArr1 dimerization. *A–C*, *left* panels show overlays of the c(s) distributions for three concentrations from each mutant xArr1 including the lowest and highest concentrations that were examined. *Right* panels show the weighted S values and fittings to the MD model, as described in Fig. 3.

Although a single Arr1 molecule was found in the asymmetric units of both crystal forms, analysis of the crystal packing environments revealed two candidate dimer interfaces, one for $xArr1_{SG1}$ involving an N-domain/C-domain (NC) interaction and the other for $xArr1_{SG2}$ involving a C-domain/C-domain (CC) interaction (Fig. 5*C*). The NC dimer interface (Fig.5, *C* and *D*, left panels) involves a parallel β-sheet interaction between the first strand on the concave face of the N-terminal domain and the first strand on the convex face of the C-terminal domain that buries 712 $Å^2$ of surface area (Fig. 5*D*, left panel). The surface is weakly hydrophobic (ΔG_i = −3.7 kcal/mol) but displays a relatively high shape complementary statistic (0.69). Similar interactions have been described in the crystal structures of Arr1, Arr2, and Arr3 (for an example, see Fig. 4 in (35)). This NC dimeric arrangement is continuously repeated by application of symmetry operations, leading to infinite chains extending through the crystal. The asymmetric and linear nature of the interaction and the consequent potential for indefinite polymer formation (36) is at odds with the exclusive monomer-dimer equilibrium observed for xArr1 in solution. Hence, this interaction may be irrelevant to the *in vitro* solution dimer (barring any negative cooperativity of association) although the fibrillar structure may be relevant in photoreceptor cells where Arr1 concentrations reach millimolar levels.

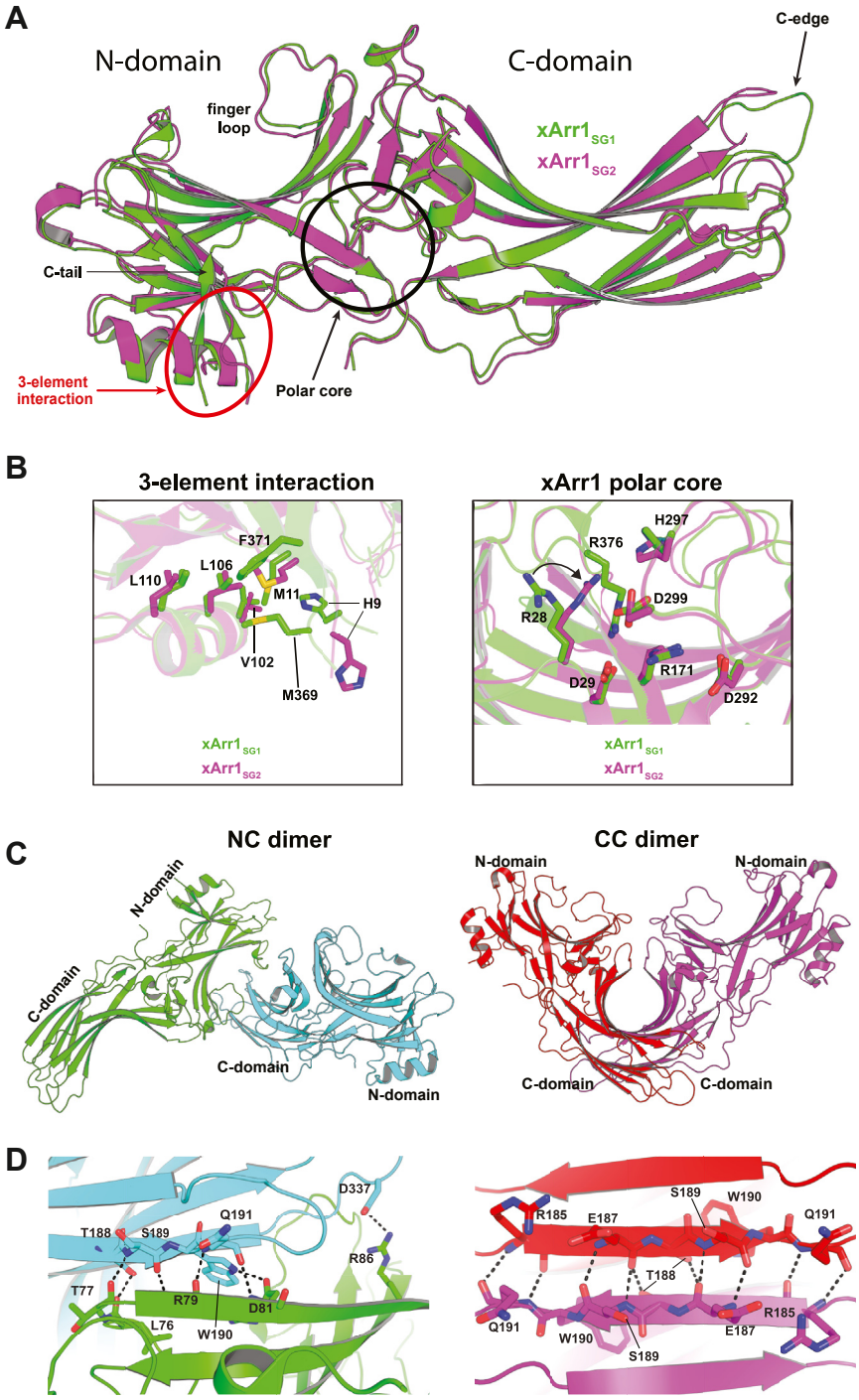

Figure 5. Comparison of two crystal structures of xArr1. *A*, global superposition of xArr1$_{SG1}$ and xArr1$_{SG2}$, highlighting the regions with significant differences. *B*, differences between xArr1$_{SG1}$ and xArr1$_{SG2}$ at the 3-element interaction (*left* panel, superposition based on residues 99–112) and the polar core (*right* panel, global superposition) regions. *C*, NC dimer of xArr1$_{SG1}$ (*left*) and CC dimer of xArr1$_{SG2}$ (*right*) found in their respective crystal lattices. *D*, details of the dimer interfaces featured in the NC (*left*) and CC (*right*) crystals. *Dashed* lines represent hydrogen bonds between monomers.

By contrast, the CC dimer found in xArr1$_{SG2}$ forms a closed, two-fold rotationally symmetrical assembly (Fig. 5, *C* and *D*, right panels) and hence lacks the potential for larger oligomer formation. Analysis of this dimer interface with the PISA server (37) showed that it is moderately hydrophobic (ΔG_i = −12.4 kcal/mol) and buries a larger surface area (1364 Å^2) as compared to the NC dimer, albeit with a lower shape correlation index (0.532). These interaction metrics are comparable to those of the established nonobligate dimer interaction formed between the alpha and beta subunits of heterotrimeric G proteins (i.e., ΔG_i = −8.6 kcal/mol with an interface area of 1145 Å^2 for $G_i\alpha,\beta$, PDB accession code: 1GP2). Most of the polar interactions sustaining the xArr1 CC dimer are hydrogen bonds between main chain atoms from

Table 2
X-ray crystallographic data collection and refinement statistics

Crystal form	$xArr1_{SG1}$[a]	$xArr1_{SG2}$
Data collection		
Beamline	NECAT ID-C	NECAT ID-E
Wavelength (Å)	0.97918	0.97918
Space group	$P3_121$	$P3_221$
Unit cell dimensions		
a, *c* (Å)	81.83, 139.62	80.77, 120.10
Resolution (Å)	50-2.54 (2.69–2.54)[b]	50-2.89 (3.07–2.89)[b]
R_{merge} (%)	14.8 (336.1)	4.9 (269.2)
$I/\sigma I$	13.47 (0.7)	21.53 (0.8)
$CC_{1/2}$ (%)	99.9 (39.3)	100 (69.4)
Completeness (%)	100.0 (99.9)	99.8 (99.3)
Multiplicity	20.1 (20.8)	9.9 (10.1)
Wilson *B*-factor (Å^2)	82	130
Refinement		
Resolution (Å)	49.73-2.54	45.56-2.89
No. of reflections	17,524 (919)[c]	10,013 (527)[c]
R_{work}/R_{free} (%)	18.9/22.9	24.9/29.6
No. of atoms	2906	2756
Protein	2884	2755
Water	22	1
B-factors (Å^2)	84.2	166.4
Protein	84.3	166.5
Water	71.6	112.4
R.M.S. deviations		
Bond lengths (Å)	0.003	0.002
Bond angles (°)	0.920	0.608
Ramachandran plot		
Favored (%)	96.1	92.3
Number disallowed	0	0
PDB accession code	8FUT	8FUU

[a] Dataset obtained by merging data from four isomorphous crystals.
[b] Highest-resolution shell is shown in parentheses.
[c] Number of reflections used for cross-validation.

strands XI in opposite monomers (Fig. 5*D*, right panel). By contrast, interactions between the top layer strands (strand XIX) in opposite monomers are mostly long range. In addition, there is one hydrogen bond between $N^{\varepsilon 1}$ W190 of strand XI from each monomer and the main chain oxygen atom from E346 of strand XIX from the opposite monomer (Fig. 5*D*, right panel). Finally, there is a close interaction between middle loop residues Ser136 and Asp137 that may influence the dimer interaction. In summary, the CC dimer is formed by an extended beta-sheet interaction (38) together with a core of principally van der Waals interactions that likely contribute to the dimer affinity. The computed biophysical characteristics of this assembly make it a plausible model for the solution dimer. Interestingly, Venn diagram analysis of residues involved in protein-protein contacts for the two identified dimer assemblies revealed a clustering of shared residues at the CC dimer interface (Fig. S1), suggesting that this region of the protein is particularly "sticky" and prone to forming protein–protein interactions. It is notable that the CC dimer assembly observed for $xArr1_{SG2}$ has never been observed previously in the crystals of vertebrate Arr1 proteins.

An overlay of xArr1 and bArr1 structures shows they are highly similar, with a few differences in the peripheral regions of the C-domain (Fig. 6*A*). Remarkably, the CC dimer form found in $xArr1_{SG2}$ is highly similar to the CC dimer predicted for mammalian Arr1 based on solution EPR and DEER spectroscopy data (23) (Fig. 6*B*). Analysis of the interface for the bArr1 solution CC dimer model with the PISA server (37) showed that it buries a slightly smaller surface area (1086 Å^2) than the xArr1 CC dimer (1364 Å^2) and is somewhat less hydrophobic (ΔG_i = −7 kcal/mol *versus* −12.4 kcal/mol). The residues predicted to be involved in the bArr1 CC solution dimer interface overlap significantly with those of the crystallographic xArr1 CC dimer and are mainly found within β-strands XI and XIX and, to a lesser extent, within the middle loop, β-strand XVI, 344-loop, and the C-terminus of loop 17 to 18 (Fig. S2). Despite this striking similarity of the dimeric structure, xArr1 failed to form tetramers, which we discuss further below.

AlphaFold3 model of xArr1

Next, we used Alphafold3 (AF3) (39) to generate dimer models of xArr1 with its protein sequence as only input. AF3's output consisted of five models of CC dimers with a similar arrangement to that of $xArr1_{SG2}$. The alpha carbon RMSD for pairwise comparisons of each dimer with the CC dimer in $xArr1_{SG2}$ ranged from 3.143 to 5.032 Å. The best fitted model (model-1) is compared to the crystallographic CC dimer of $xArr1_{SG2}$ in Fig. S3. Both models overlay relatively well, with some differences in the position of the loops and a general agreement in the secondary structure (Fig. S3*A*). The only major difference between the two models is at the C-tail, since in the AF3 model-1 is predicted to fold as an α-helix contacting the concave side of the N-domain, while in the $xArr1_{SG2}$, the C-tail is disordered and disengaged from the N-domain. The remarkable agreement in the dimer arrangements, especially at the monomer–monomer interface between residues R185 and Q191 (Fig. S3*B*), provides an additional argument supporting the physiological relevance of $xArr1_{SG2}$'s CC dimer.

Key differences in the xArr1 CC dimer structure may explain the disparate levels of oligomerization found for xArr1 and bArr1

An important difference between the crystal xArr1 CC dimer structure and the predicted solution structure of bArr1 is that F193 in xArr1, which is homologous to the F197 residue in bArr1 found to be crucial for CC dimer formation, is located outside of the predicted β-sheet dimer interface (Fig. 7*A*). This difference in position may explain why the F193A substitution did not reduce xArr1 dimer affinity as shown in Fig. 4.

A second key difference in the predicted CC dimer structures lies in the orientation of the N-domains. In bArr1, the N-domains in the CC solution dimer appear flatter relative to one another (Fig. 7, *A* and *C*), and the predicted bArr1 tetramer showed an NN interaction surface involving F85 (Fig. 7*C*, left panel). Interestingly, replacing F85 with a cysteine containing a nitroxide side chain spin label led to a significantly lower bArr1 M-D association constant and complete loss of tetramer formation (16, 23). The flatter orientation of the N-domains potentially allows efficient interactions between the four N-domains of the CC dimers. The xArr1 structure, on the other hand, shows an interdomain rotation, such that all four N-domains are not allowed to simultaneously form NN

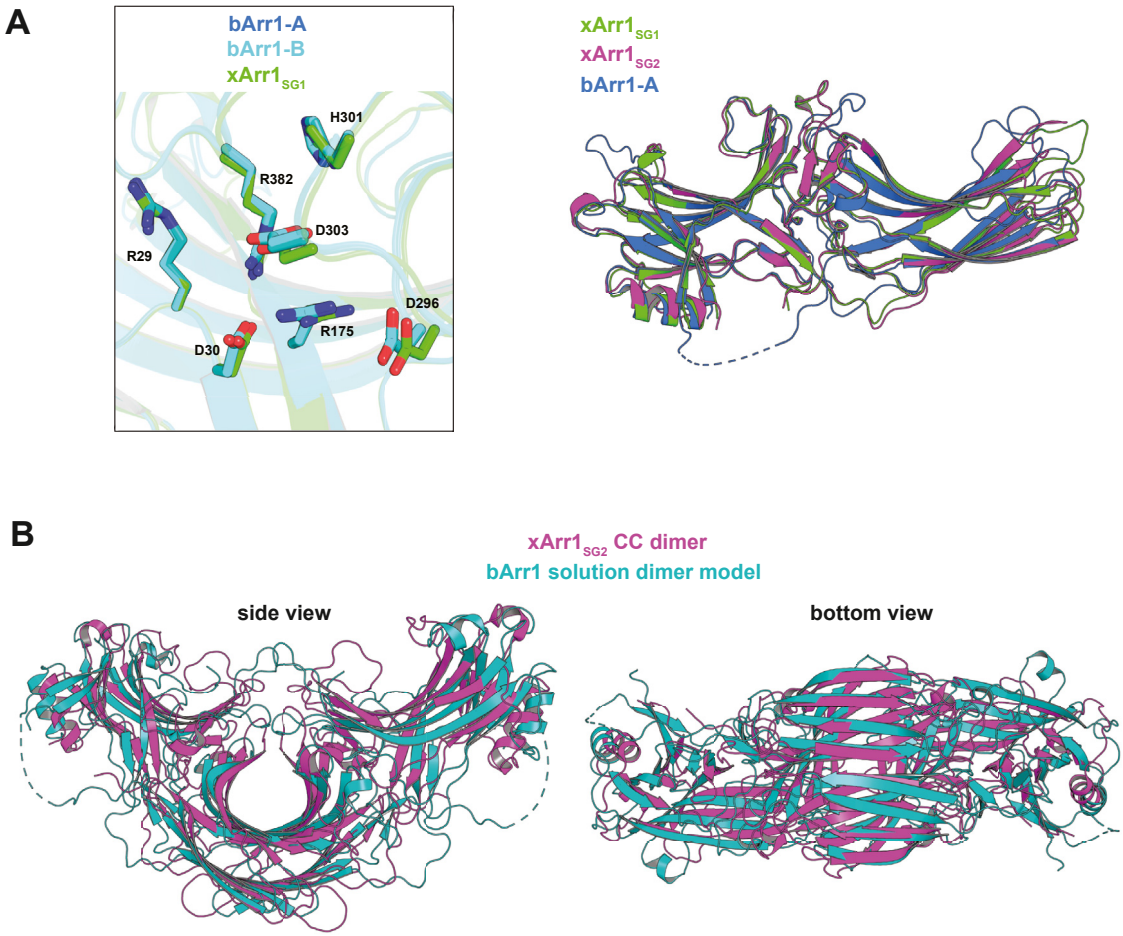

Figure 6. Comparison between structures of bArr1 and xArr1. *A*, global superposition of the polar core in basal bArr1 (PDB ID 7JSM, chains *A* and *B*) with xArr1$_{SG1}$ (*left* panel). Residue numbering is based on the bArr1 sequence. Global superposition of xArr1$_{SG1}$, xArr1$_{SG2}$, and basal bArr1 (PDB ID 7JSM, chain *A*) (*right* panel). *B*, global superposition of the CC dimer of xArr1$_{SG2}$ with the CC dimer of bArr1, extracted from the solution tetramer model (23).

interactions (Fig. 7, *B* and *C*). Moreover, mutation of the orthogonal Y84 (Fig. 7*C*, right panel) in xArr1 had no impact on xArr1 oligomerization (not shown). This difference in quaternary structure provides a possible explanation for the lack of xArr1 tetramer formation: binding between one pair of the N-domains in interacting CC dimers prevents efficient binding of the other N-domain pair.

Mutagenesis of residues within the putative xArr1 dimer interfaces modestly reduces dimer formation

The xArr1 crystal structures provide maps of residues predicted to be involved in two possible dimer interfaces. This allowed us to devise systematic mutagenesis experiments to evaluate the roles of these residues in dimer formation. In the CC dimer, residues within the closely apposed β-sheets (corresponding to strand XI from Fig. 1) (Fig. 8*A*) closely resemble the key CC dimer interface in the bArr1 solution model (23). We thus replaced residues 188 to 191 (Fig. 8*A* lime) with alanines (xArr1(T188-Q191A)). Importantly, residues T188-Q191 are also predicted to be involved in the NC dimer interface (Fig. 8*C*), thus mutation of these residues is predicted to influence both CC and NC dimer affinities, if the crystal structure indeed is predictive of the dimer interface. This mutant arrestin dimerized with ∼ 3.5-fold lower affinity, K_D = 183 μM (Fig. 8*D* upper isotherm), than that of the WT protein, K_D = 52.8 μM (Fig. 2), a difference that was significant at the p = 0.05 level (Table 1), albeit modest.

We then examined the impact of mutating residues 182 to 185 (Fig. 8*A* cyan) in addition to residues 188 to 191 (xArr1-P182-R185A;T188-Q191A). This strategy allowed complete disruption of the entire β-sheet interaction side chains without losing structural integrity of the molecule. Surprisingly, the dimer affinity of this mutant, K_D = 74.2 μM (Fig. 8*D*), marginally reduced relative to that of WT, did not reach statistical significance (Table 1).

Another possible dimer interface domain predicted from the crystal structure are residues S136 and D137, which are part of the middle loop, one of several flexible loop structures thought to be involved in P-Rho binding (40). Replacing these residues with alanines marginally decreased the K_D to 20.2 μM, although the difference did not reach significance (Fig. 8*D*, Table 1). These two polar residues are accessible to water in the xArr1 CC dimer and, therefore, the contribution of the

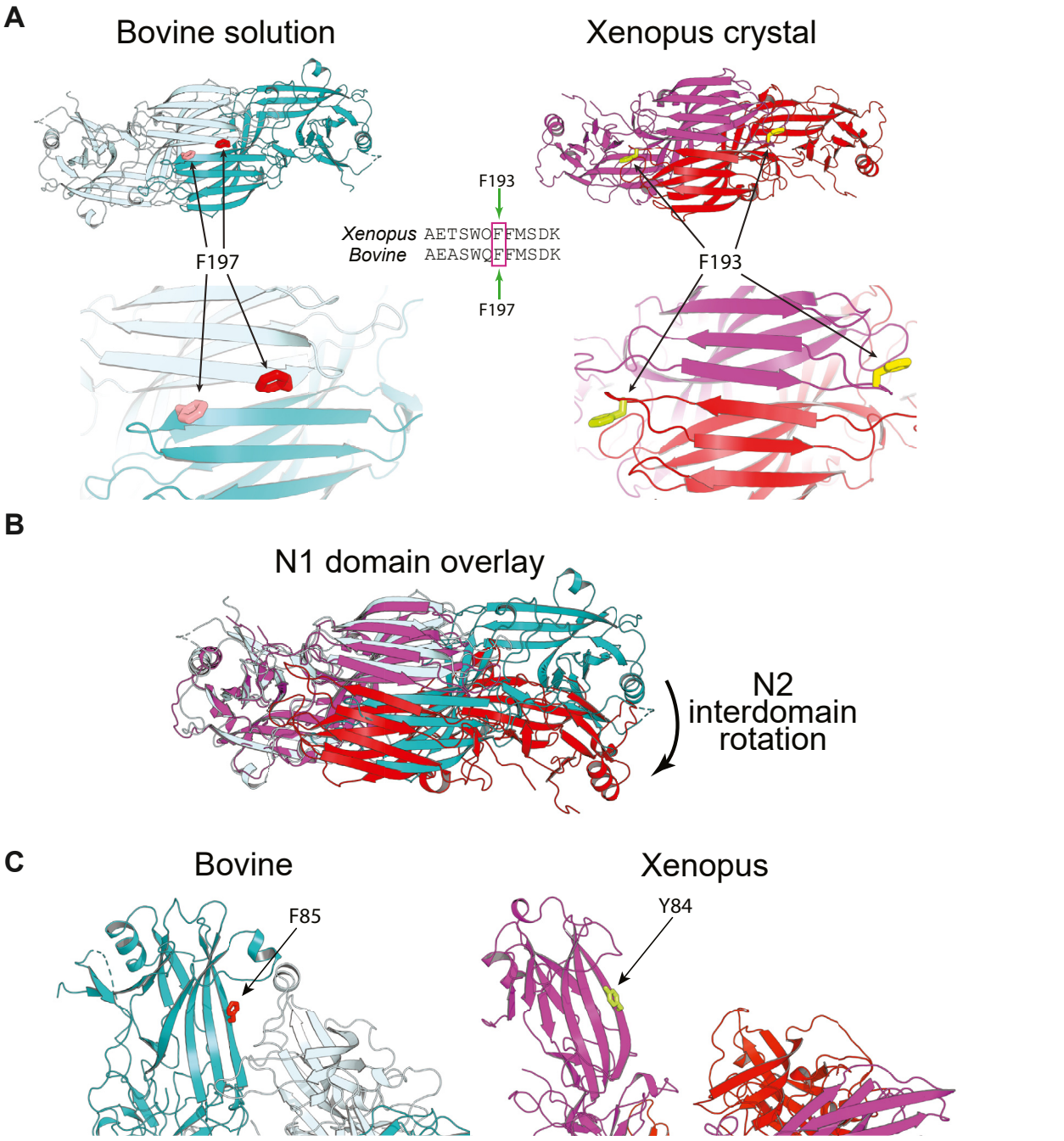

Figure 7. Differences between bArr1 and xArr1 CC dimers. *A*, position of F197 in the CC dimer solution model of bArr1 (23) (*left* panel) compared to the corresponding F193 in the CC dimer of $xArr1_{SG2}$ (*right* panel). The side chain atoms for xArr1 F193 were omitted from the final model owing to weak electron density but are shown here in a geometrically reasonable position for illustrative purposes. *B*, bArr1 CC dimer predicted from the solution tetramer model (23) and xArr1 crystallographic CC dimer. Overlaying the N-domains of one monomer from each dimer reveals a differential rotation of the opposite N-domains, showing that an xArr1 tetramer with the same arrangements as the bArr1 tetramer would not be possible. *C*, position of F85 in the solution tetramer model of bArr1, at the interface between the N-domains of adjacent dimers (*left* panel). The *right* panel shows the positioning of xArr1 Y84 relative to the opposing N-domain when two $xArr1_{SG2}$ dimers are superimposed onto the bArr1 solution structure (superposition based on a single chain of the dimer). This comparison suggests that the differing orientation of the xArr1 CC dimer could prevent the tetramerization observed for bArr1. Complete models are shown in Fig. S5.

hydrogen bonds between S136 and D137 to dimer stability is, not surprisingly, negligible. On the contrary, their substitution by alanine might enhance dimerization to bury these apolar side chains.

Finally, four residues in addition to T188-Q191 are predicted by the crystal structure to be involved in the dimer interface: L156, E157, D337, and S340 (Fig. 8*D*). Mutation of these four residues to alanines along with T188-Q191 (xArr1-L156A, E157A, T188-Q191S, D337A, S340A) resulted in a dramatic and significant increase in dimer affinity, K_D = 4 μM, rather than a decrease (Fig. 8*D*, Table 1).

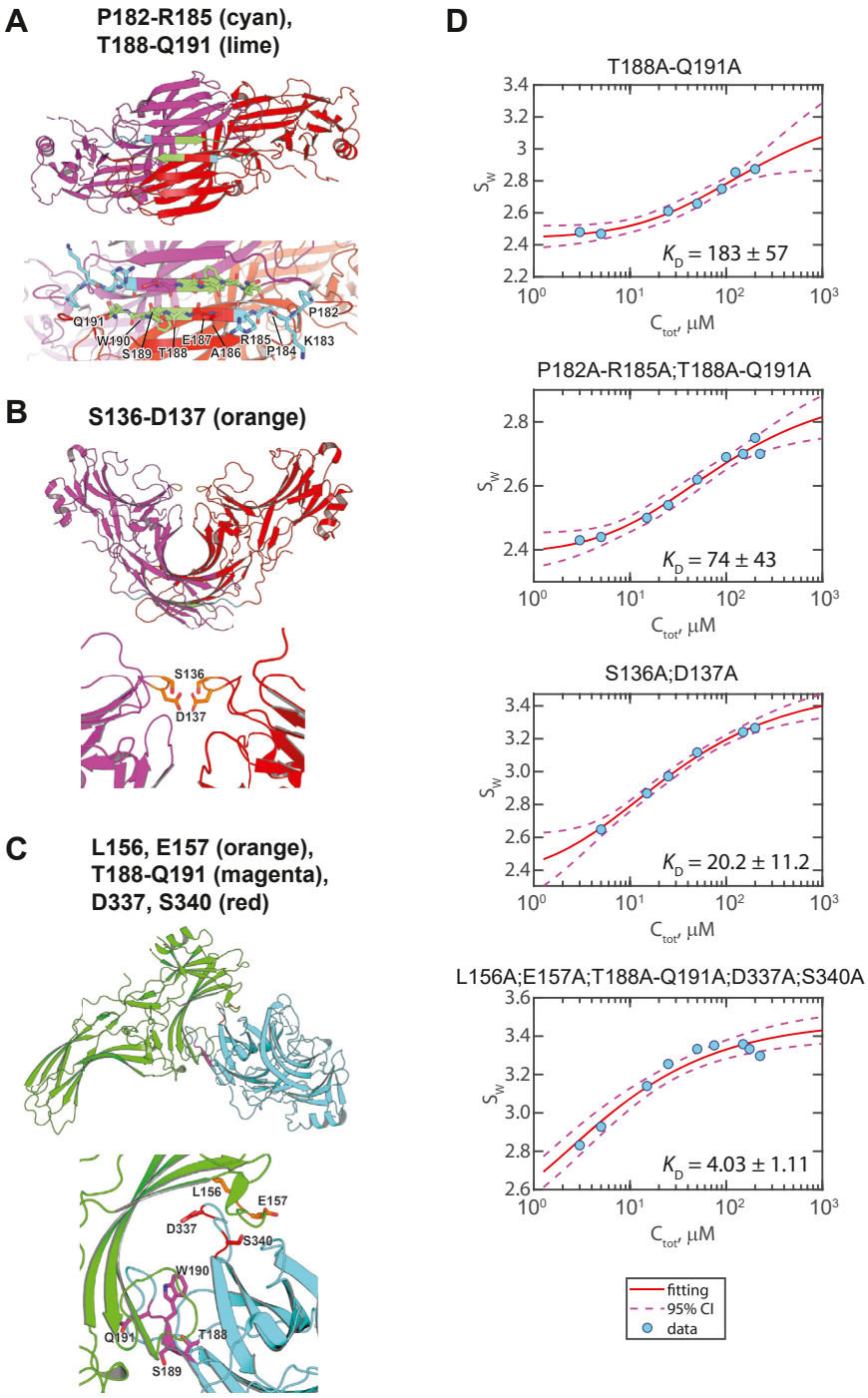

Figure 8. AUC SV analysis of xArr1 mutants designed based on the two xArr1 crystal structures. *A*, position of residues P182-R185 (*cyan*) and T188-Q191 (*lime*), from strand XI and adjacent loops, in the context of the xArr1 CC dimer. *B*, position of residues S136-D137 from the middle loop, in the context of the xArr1 CC dimer. *C*, position of residues L156, E157, T188-Q191, D337, and S340 in the context of the xArr1 NC dimer. *D*, monomer-dimer isotherm fittings of the weighted S values from AUC SV analysis of the indicated xArr1 mutants. Solid *red* lines are fittings and dashed *magenta* lines are 95% confidence boundaries. Fitted K_D values are shown.

SAXS analysis of xArr1 at various concentrations indicates the solution structure of xArr1 differs from those predicted from crystal structures

The modest impact of mutagenizing residues at the dimer interfaces predicted from the crystal structures suggests that these interfaces may not be the only or even the predominate mechanism for xArr1 dimer formation in solution. To examine this possibility, we evaluated the solution structure of xArr1 at various concentrations using SAXS. Recombinant xArr1 concentrations between 0.25 and 7.6 mg/ml (∼5.2–158 μM) were analyzed using the ATSAS suite (41) in quadruplicate and averaged (Fig. 9). Analysis of Guinier plots with PRIMUS and GNOM (Fig. 9, *A* and *B*) showed that the radius of gyration (Rg) of xArr1 increased ∼1.4-fold and the molecular mass (by

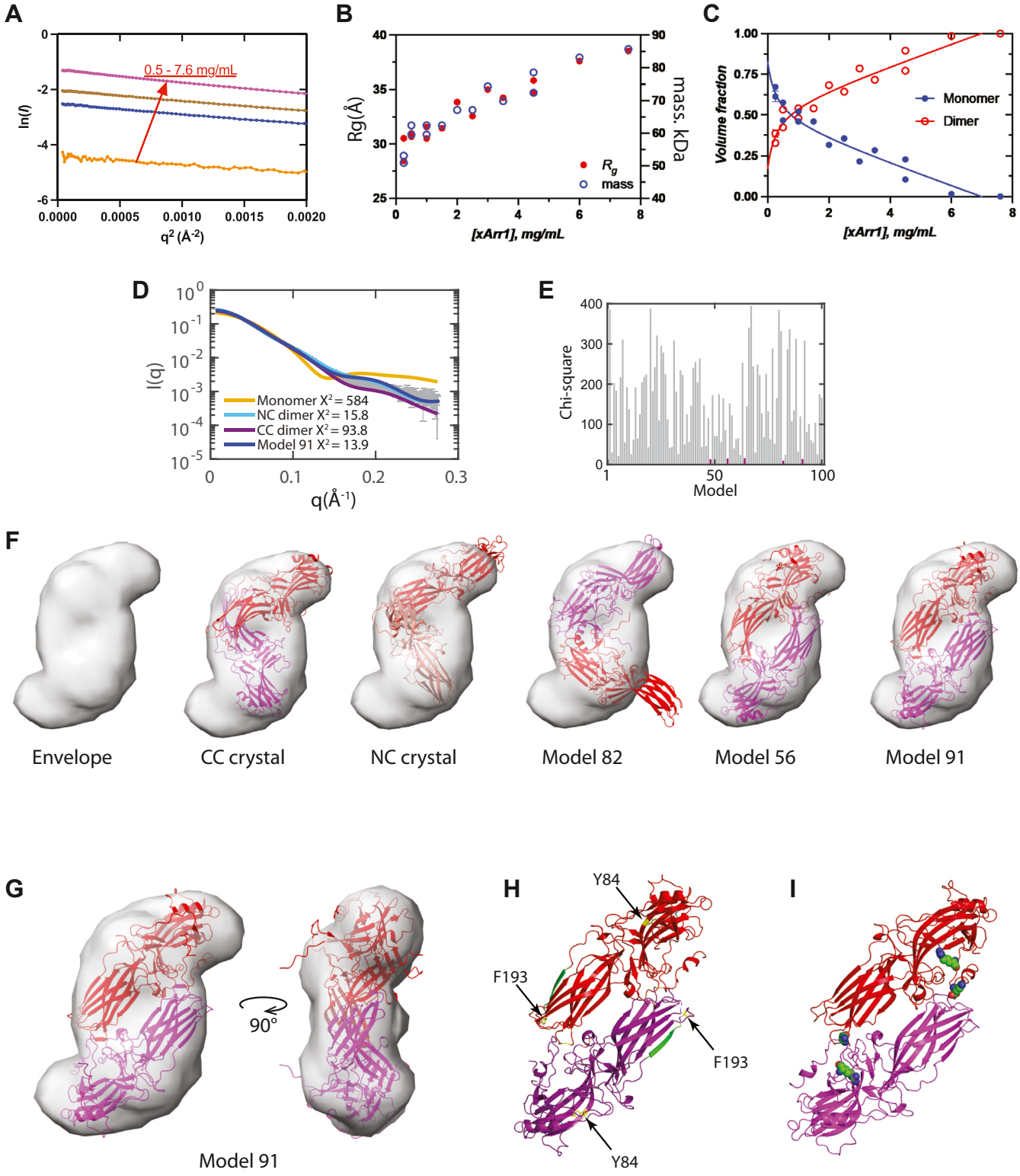

Figure 9. SAXS analysis of xArr1 reveals the solution dimer structure differs from the predicted crystal dimers. *A*, Guinier plot of xArr1 at 0.5, 2, 4.5, and 7.6 mg/ml. *B*, radius of gyration (Rg) and mass as predicted by Bayesian inference from scattering analysis from indicated xArr1 concentrations. *C*, monomer and dimer volume fraction determined from PRIMU and GNOM. Lines represent fittings to a monomer-dimer binding isotherms with $K_D \sim 20$ μM. *D*, I(q) plots from monomer and NC and CC dimers and dimer model 91 predicted from the crystal structure of xArr1 using Crysol. Model 91 has the lowest χ^2 value suggesting it provides the best fit. *E*, bar chart of χ^2 values from 100 models of the xArr1 dimer generated by SASREF and analyzed by Crysol. The five models generating the lowest χ^2 are highlighted in *magenta*. *F*, *Ab initio* model of the SAXS envelope generated in GASBOR. The *left*-most panel shows the envelope alone and each of the other panels is a fitting of the indicated model into the envelope using the UCSF ChimeraX fit function. *G*, enlarged envelope with model 91 displayed in two views shows the best fitting. *H*, model 91 with crystal predicted dimerization interface residues highlighted in *green*, *cyan*, and *yellow*. Residues Y84 and F193 that were identified as important for bArr1 oligomerization are indicated. *I*, model 91 with R375 and K379 identified in protein painting/mass spectrometry are found on the putative antiparallel dimer interface.

Bayesian inference) increased ~1.6-fold over this range of concentrations, (Fig. 9*B*). These results are in good agreement with the results obtained with AUC above. The volume fraction of monomer and dimer, as determined by predicted scattering of the monomer and dimer models generated by SASREFMX and analyzed by OLIGOMER, predicted higher affinity binding than estimated from AUC analysis, K_D ~ 20 μM (Fig. 9*C*), a difference that was not statistically significant.

Comparison of the crystal-predicted scattering of monomer and CC and NC dimers of xArr1 to the scattering data of xArr1 at 7.6 mg/ml using CRYSOL shows that the NC dimer best fitted the experimental scattering (Fig. 9*D*). However, the χ^2 ~ 16 of the fitting suggested that the NC dimer may not fully describe the solution structure of the xArr1 dimer. The *ab initio* molecular envelope calculated with GASBOR at the highest concentration, which encompassed nearly 100% dimer, suggested C2 symmetrical symmetry. We therefore used SymmDock to generate possible dimer models with cyclic symmetry and evaluated them in Crysol to search for structures that provided a better fitting of the I(q) scattering data. One hundred xArr1 dimer structures were generated and fitted to the scattering data with Crysol, yielding broadly scattered χ^2 values (Fig. 9*E*). The five best models fitted the I(q) curve with χ^2 values below 20, ranging from 9.6 to 15.7, were indistinguishable from each other based on this criterion (Fig. 9*E* red bars).

To further characterize the models, an *ab initio* reconstruction of the scattering envelope was generated using GASBORMX. The three best fitting structures, as well as the NC and CC dimers from the crystal structures, were then fitted to the SAXS envelope generated by GASBORMX using the fit function in UCSF ChimeraX (Fig. 9*F*). Of these, models 56 and 91 provided the best fitting to the SAXS envelope (Fig. 9, *F* and *G*). For comparison, the dimer interfaces predicted by the CC and NC dimers from the crystals are highlighted (Fig. 9*H*, green shading). Importantly, the large β-sheet interaction surface predicted by the CC structure and weakly implicated in mutagenesis experiments are not shown to interact in models 56 and 91.

To further evaluate the solution dimer models, we performed protein painting mass spectrometry (Fig. 9*I*). This approach identifies trypsin cleavage sites that are solvent inaccessible at the dimer interface. Arr1 at a concentration of 0.4 mg/ml was incubated with the dye disodium; 1-amino-9,10-dioxo-4-[3-(2-sulphonatooxyethylsulphonyl) anilino] anthracene-2–sulphonate (RBB). Arr1 is then denatured and subjected to trypsin digestion and the resulting peptides were identified by mass spectrometry. RBB binds to the solvent accessible surfaces, protecting them from trypsin digestion, thus only the residues lacking RBB paint are digested. We detected two peptides at the C-terminus of Arr1 cleaved at arginine residue 375 and lysine residue 379 in our painted sample that are located on the interface between the xArr1 antiparallel dimer model 91 (Fig. 9*I*, spheres). Together, these results suggest that the xArr1 solution dimer strongly favors an antiparallel (AP dimer) structure similar to model 91, although it cannot be ruled out that multiple competing dimer forms of xArr1 may exist in solution.

Roles of steric volume exclusion-mediated partitioning and binding to cell body–localized partners in the depletion of Arr1 from the outer segment

We evaluated the impact of xArr1 dimerization and binding to inner segment partners on its distribution in dark-adapted rods. Under dark-adapted conditions, xArr1 is roughly uniformly distributed within the cytoplasmic of the inner segment/cell body and presynaptic spherule, while being depleted from the outer segment. (17, 24, 25, 42–47). A convenient way to quantify the distribution is to take the ratio of the average concentration, relative to the plasma membrane envelope, within the outer segment and the myoid region of the inner segment ($R_{OS/IS}$). Analysis of Arr1 distribution patterns in dark-adapted rods from published data using this approach shows that the $R_{OS/IS}$ ranges from 0 to 0.2 (17, 24, 43, 48). The mechanisms underlying this distribution remain unsolved; however, two primary hypotheses have been posited. In the first, depletion of Arr1 from the outer segment was proposed to operate through an inner segment binding sink (19, 49); an idea originating with the identification of several inner segment Arr1-binding partners, including tubulin (19, 49), enolase1 (18), N-ethylmaleimide-sensitive fusion protein (20), and the BBSome protein BBS5 (50). In the second mechanism, Arr1 partitioning into the inner segment was proposed to operate via a steric volume exclusion-mediated mechanism (17) that relies on the dramatic structural heterogeneity between the cytoplasm of the outer segment, which is crowded with disc membranes spaced ~12 to 15 nm apart (51–53) and that of the less crowded inner segment/cell body. Here we leverage our computational diffusion and binding model that accounts for the available volumes in photoreceptor compartments (54) to evaluate the proposed mechanisms based on experimentally measured parameters.

First, we evaluated the inner segment binding sink hypothesis. We chose to model two prototypical inner segment binding partners (ISBPs) for xArr1, tubulin with K_D ~ 40 μM for mammalian Arr1 binding to αβ tubulin dimers and assembled microtubules (55) and enolase 1 with an Arr1 binding K_D ~ 1 μM (18). In this analysis, we ignored the steric volume exclusion-mediated partitioning and uniformly distributed the immobile prototypical ISBPs throughout the inner segment/cell body and presynapse (Fig. 10*A*). The geometries of these compartments, and hence their volumes, were set to realistic *Xenopus* rod photoreceptor dimensions and the concentration of xArr1 was set such that it was 2.4 mM relative to the outer segment plasma membrane envelope, reflecting the ~ 1:0.8 rhodopsin:arrestin ratio in rods (48). The distribution of xArr1 calculated at four concentrations of tubulin in the inner segment are shown in the lower panels of Fig. 10*A*. The outer segment enrichment indices, $R_{OS/IS}$, for a range of ISBP concentrations and K_Ds are plotted in Fig. 10*B*. Under these conditions, our model shows that the concentration of tubulin in the cell body required for a tenfold

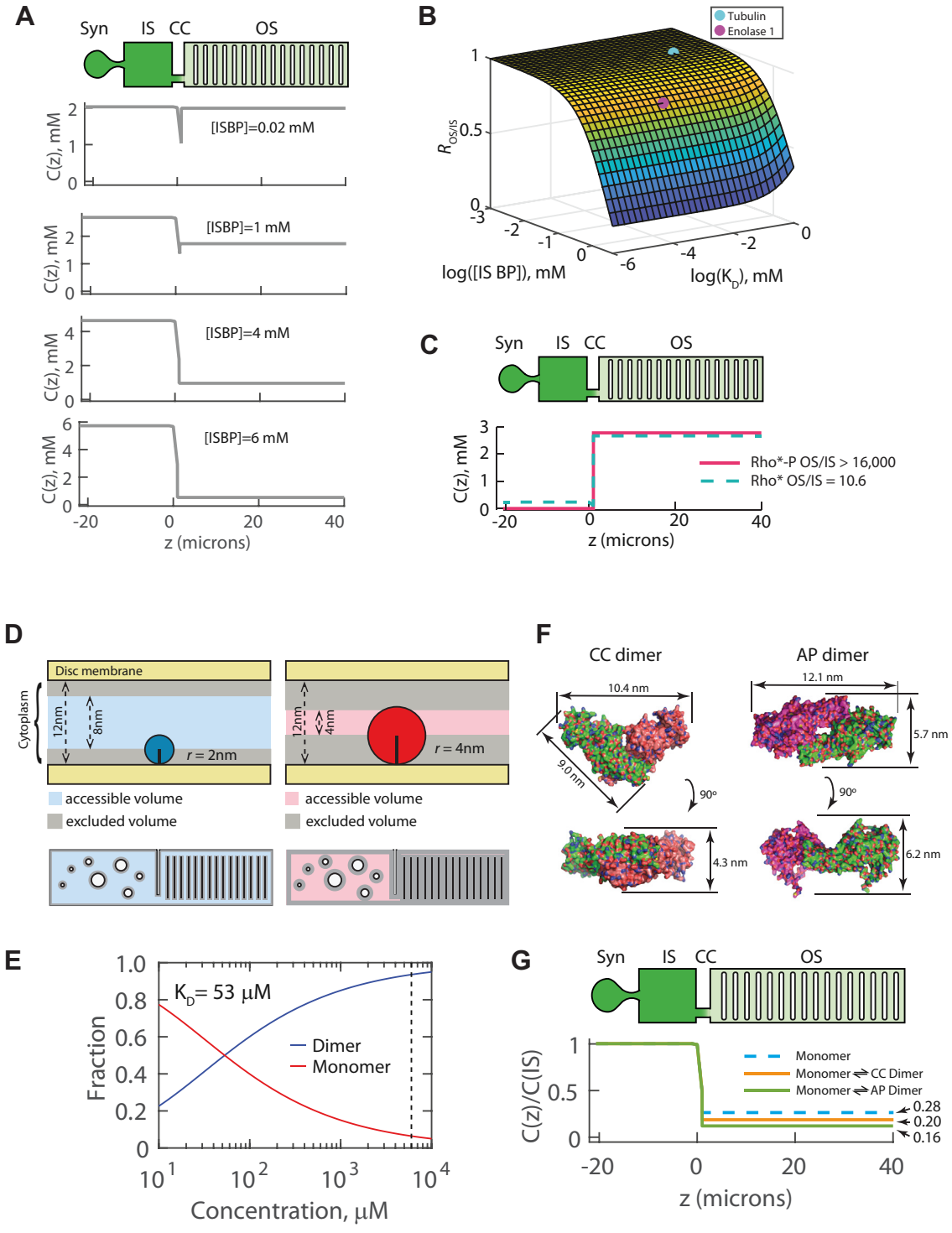

Figure 10. Evaluation of the relative impact of inner segment binding partners and partitioning by steric volume exclusion on the depletion of xArr1 from the outer segment of dark-adapted rods. *A*, the *top* panel is a schematic of a rod. *Lower* panels represent computed concentration distributions of Arr1 in photoreceptors with indicated concentration of a prototypical inner segment binding partner (ISBP). The average Arr1 concentration, relative to the plasma membrane envelope, was 2 mM. ISBP was treated as an immobile binding partner present only in the Syn and IS, with Arr1 binding K_D = 40 μM, which corresponds to bArr1 binding to tubulin dimers and microtubules (55). An ISBP concentration of 6 mM was required to achieve an OS/IS concentration ratio, $R_{OS/IS}$ = 0.1. *B*, plot of the relationship between the OS enrichment index ($R_{OS/IS}$), the K_D of the ISBP binding with xArr1, and the IS concentration of the ISBP. The *cyan* symbol indicates the predicted $R_{OS/IS}$ for tubulin interactions (59, 60). The *magenta* symbol indicates the predicted $R_{OS/IS}$ for Arr1 binding to enolase 1, with $K_D \sim 1$ μM and inner segment concentration of $\sim$ 0.4 μM (see text for details). These results show that physiological concentrations of tubulin would produce negligible partitioning of Arr1 to the cell body and pre-synapse whereas enolase 1 would be expected to produce 20% IS localization provided that enolase 1 is indeed present at 0.4 μM concentration in the IS, a value that is currently undetermined. *C*, predicted distributions of Arr1 in rods where all rhodopsins are light activated with or without phosphorylation (Rho*-P or Rho*, respectively). In either case, Arr1 is predicted to be strongly localized to the outer segment, where the localization is essentially quantitative for Rho*-P and produces ~10 fold enrichment for Rho*. *D*, schematic representation of the steric volume exclusion effect within the interdiscal space (*upper* panels) and the photoreceptor overall (*lower*

difference in OS-IS concentrations is on the order of 6 mM (Fig. 10, *A* and *B*), a concentration that is 2-3-fold higher than that of rhodopsin or Arr1, the most abundant proteins in photoreceptors by a margin of tenfold above the next most abundant protein complex, transducin (15, 48, 56–58). The concentration of tubulin in photoreceptors has not, to our knowledge, been quantified. However, the tubulin concentration in cultured neurons was found to be 5 to 20 μM (59, 60), orders of magnitude below that required for photoreceptor cell body localization of Arr1 (Fig. 10*B*, cyan symbol). Indeed, even if the concentration of tubulin in photoreceptor were 200 μM, tenfold higher than reported in cultured neurons, our calculations show that the binding sink would maximumly account for ∼ 10% of the cell body enrichment of Arr1 (Fig. 10*B*). Enolase 1, on the other hand, has higher affinity binding and is reported to be expressed in the whole mouse retina at a stoichiometry of 0.5:1 enolase 1:Arr1 (61). While the rod-specific expression of enolase 1 is not known, even if we assume all of it is expressed in rod cell bodies, the model predicts that it would account for only ∼ 20% of the cell body enrichment of Arr1 (Fig. 10*B*, magenta symbol). Thus, low affinity inner segment binding sinks cannot explain Arr1 enrichment in the photoreceptor cell body, irrespective of whether it is made up of one or several known Arr1-binding partners.

To examine the hypothesis that Arr1 localization to the outer segment of light-adapted rods is due to a binding sink created by photoactivated and phosphorylated rhodopsin (Rho*-P), we evaluated models where binding partners were uniformly distributed in the outer segment compartment (Fig. 10*C*). Two cases were examined: Arr1 binding to Rho*-P and Arr1 binding to light-activated, unphosphorylated rhodopsin (Rho*). In both cases, we set the Rho* concentration to be 6 mM, the disc-excluded concentration of rhodopsin in the outer segment. We set the Arr1:Rho*-P K_D = 20 nM (62) and the Arr1:Rho* K_D = 200 μM, within the K_D range of 150 to 300 μM for Arr1:Rho* binding estimated by NMR (56). Remarkably, the outer segment enrichment of Arr1 is predicted to be significant in either scenario. The high affinity between Arr1 and Rho*-P drives essentially complete localization of Arr1 to the outer segment with an $R_{OS/IS} > 40{,}000$. Alternatively, the 10,000-fold lower affinity binding between Arr1 and unphosphorylated Rho* is predicted to result in an $R_{OS/IS} > 10$. While the difference in these enrichment factors is large, as expected for the large difference in binding affinity, it should be noted that the Arr1 distribution in rods as measured by traditional immunohistochemistry approaches would be hard pressed to detect it. These results, thus, refute previous conclusions that diffusion to a Rho* binding sink could not explain outer segment localization of Arr1 in the absence of Rho* phosphorylation, which were used as evidence for active Arr1 transport (43). Our results for the Arr1:Rho* binding sink analysis highlight the value of computational modeling in correctly interpreting experimental results.

We next evaluated the steric volume exclusion-mediated partitioning mechanism (Fig. 10*D*). The chief compartments of photoreceptors possess dramatic structural heterogeneity of the cytoplasm, where the ciliary outer segment is filled with membranous discs spaced at a highly regular ∼ 12 nm (51, 63, 64), which stands in stark contrast to the much less structured cytoplasm of the cell body (64). Our prior work directly showed that this heterogeneity significantly impacts the distribution of soluble molecules in a size-dependent manner (17). The mechanism dictates that soluble molecules will be at the same concentration, relative to the local volume accessible to their centers of mass, everywhere in the aqueous cytoplasm. But because of the close juxtaposition of the discs in the outer segment, which is connected to the less structured cell body by the connecting cilium, the soluble molecules will partition into the cell body owing to its larger accessible volume. This means that the mass density (concentration) of molecules, relative to the plasma membrane envelope volume, is higher in the cell body than in the outer segment, even though the effective concentrations relative to the accessible aqueous volume in these compartments are the same.

Based on the K_D of ∼53 μM for xArr1 dimer formation and the 4.8 mM concentration of xArr1 relative to the disc-excluded cytoplasm, which follows from the Arr1:rhodopsin stoichiometry of 0.8:1 (48), more than 95% of xArr1 will be in the dimer form in dark-adapted rods (Fig. 10*E*). The crystal structure-predicted xArr1 CC dimer shape approximates a 4.3 nm thick triangle 9 nm along the sides comprised of each of the proteins and ∼10.4 nm to the extremes of the N-termini of the molecules (Fig. 10*F* CC-dimer). The shape of the antiparallel dimer structure predicted from SAXS and protein painting MS results approximates an elliptical torus ∼12.1 nm at the widest dimension, ∼5.7 nm at the narrowest, and ∼6 nm thick (Fig. 10*G*, AP-dimer). Thus, the dimensions of xArr1 and its predicted dimer forms are on the order of the ∼ 12 nm space between outer segment disc membranes. We previously established an approach for estimating the average interdiscal volume accessible to molecules of arbitrary shape (17). Employing this approach leads to prediction of the steric volume exclusion-driven partitioning of xArr1 monomers and dimers in dark-adapted rods with dimers predicted to distribute with a $R_{OS/IS}$ of ∼ 0.2 for the CC-dimer and 0.16 for the AP-dimer (Fig. 10*G*), within the observed distribution

panels), for two molecules with different hydrated radii. The excluded volume refers to the volume near cell structures that is inaccessible to the centers of mass of soluble molecules. In geometrically constrained spaces, like the interdiscal spaces, the excluded volume significantly reduces the volume available and thus increases the effective concentration of the molecules. Larger molecules experience this effect more acutely than smaller molecules; however, the effect impacts *all* molecules. *E*, plot of fractions of xArr1 monomer (*red*) and dimer (*blue*) as a function of concentration assuming K_D = 53 μM. *Dashed* lines indicate the concentration of Arr1 (relative to momomer) in the subcellular structure-excluded cytoplasm when expressed at WT levels (4 mM). *F*, solvent accessible surface of xArr CC dimer predicted from $xArr1_{SG2}$ crystal and the antiparallel dimer (AP dimer) with dimensions. *G*, predicted distribution of monomer and dimer xArr1s in a rod based on the size and shape as computed in Najafi *et al.* 2021 (17). Note that even monomer xArr1 is strongly partitioned to the cell body. The CC dimer and AP dimer models distributions differ ∼1.2-fold while the monomer and AP dimer distributions differ ∼1/75-fold. The results show that increasing the size of Arr1 by dimerization with the K_D measured here is expected to enhance the cell body enrichment by ∼ 8 to 12%. Syn, presynaptic spherule; IS, inner segment/cell body; cc, connecting cilium; OS, outer segment.

range measured experimentally. Importantly, the analysis shows that monomer xArr1 is predicted to have a $R_{OS/IS}$ of ~0.28. Thus, most of the cell body enrichment of xArr1 is explained by steric volume exclusion-mediated partitioning of Arr1 between the major photoreceptor compartments, even if it is present only as monomers *in vivo*. Dimer formation is expected to enhance inner segment localization up to ~1.75-fold.

Discussion

Our results show that both recombinant *X. laevis* and *A. tigrinum* Arr1 self-associate in a concentration-dependent manner, thus extending *in vitro* observations of visual Arr1 oligomerization behavior to nonmammalian vertebrates. However, in contrast to bovine, mouse, and human Arr1s which have all been shown or projected to form dimers and tetramers at physiological concentrations (22), the highest observed oligomer of amphibian Arr1 are dimers. This result is somewhat surprising given the similarity in tertiary structure between xArr1 and bArr1 and raised a number of questions about the mechanisms of xArr1 oligomerization and its functional role in amphibian rod photoreceptor physiology, including whether xArr1 and mammalian Arr1s form dimers by a common mechanism and the impact of xArr1 being constrained to dimers on its function.

xArr1 likely forms dimers at multiple binding interfaces

The two crystal structures of xArr1 show a similar tertiary structure to that of bArr1, however, they predict differing dimer interfaces. The $xArr1_{SG1}$ structure features an NC dimer that is similar to those observed in crystal structures for other arrestin family members, including bArr1. The $xArr1_{SG2}$ structure features a CC dimer that has not been obtained previously in arrestin crystals. The predicted xArr1 CC dimer is remarkably similar to the solution bArr1 dimer interface predicted from EPR and DEER spectroscopy (23), and the models predicted by AlphaFold3, and it is thus tempting to conclude that this is the primary form of the xArr1 dimer. In support of this notion, the predicted CC dimer potentially explains why mutation of xArr1_Y84A/F193A, analogs to key hydrophobic residues that are important for mammalian Arr1 dimerization and tetramerization, did not reduce the ability of xArr1 to form dimers since in the predicted xArr1 dimer structure, F193 lies outside the β sheet interaction interface.

However, despite the similarities in predicted CC dimerization interfaces between xArr1 and bArr1, alanine substitution of the majority of the amino acids involved in the crystal-predicted xArr1 CC dimer interface (T188A-Q191A) had modest impact on dimerization, increasing the K_D ~3.5-fold. By contrast, mutation of only two phenylalanines in bArr1, bArr1(F85A,F197A), increased the bArr1 dimerization K_D ~twelvefold (22). Moreover, amino acids T188-Q191 are also shown to interact in the NC dimer predicted from the $xArr1_{SG1}$ crystal structure. Thus, the xArr1(T188A-Q191A) mutant, alone, cannot distinguish between the predicted CC and NC dimers. Mutagenesis of other amino acids predicted to interact in the xArr1 CC and NC dimers, including xArr1(S36A-D137A), residues found in the middle loop that are predicted to interact in the CC dimer, and xArr1(L156A,E157A,T188A-Q191A,D337A,S340A), which in addition to residues T188-Q191 includes several other amino acids predicted to interact in the NC dimer, appeared to increased xArr1 binding affinity. Finally, SAXS and protein paint MS analyses strongly support an antiparallel xArr1 dimer structure that is different not only from the crystal CC and NC dimers but from any other predicted visual arrestin dimer structure reported to date. These results suggest that dimerization of xArr1 likely occurs at multiple, competing interfaces and that the mutagenesis experiments result in shifting preference among them, but that the anti-parallel dimer is likely the predominant form in solution.

Do all mammalian Arr1s form tetramers?

The notion that mammalian Arr1s form tetramers remains controversial. The first observations that showed bArr1 self-association were made in the late 1970s while characterizing one of the antigens involved in experimental allergic uveitis (9) that was later identified as Arr1. Sedimentation equilibrium and sedimentation velocity approaches showed two species with molecular weights corresponding to monomers and dimers. Later, Shilton *et al.* (11) used SAXS to examine the shape of bArr1 in the monomer and dimer forms. They estimated the $K_{D,dimer}$ to be 60 μM and, based on the high physiological concentration of bArr1 in rods, concluded that the dimer is likely the predominant physiological form. Finally, Imamoto *et al.* (12) repeated the SAXS experiments and showed that high salt concentration used previously inhibit bArr1 tetramer formation and that at physiological salt concentrations bArr1 existed in an equilibrium between monomer and tetramer with very little dimer.

Seeking to resolve the conflicting conclusions, Hanson *et al.* (16) used MALS and EPR to examine mammalian Arr1 oligomerization. Their results supported the concentration-dependent formation of bArr1 dimers and tetramers, leading to a monomer-dimer-tetramer model of mammalian Arr1 oligomerization. They used EPR and DEER to identify residues at oligomeric interfaces and showed that they did not match the crystal tetramer and put forward a model of bArr1 oligomerization where dimers are first formed through interactions at the C-termini and tetramers formed by N-terminal interactions of the dimeric proteins. Nevertheless, a recent study examining the structure of bArr1 polar core mutant R175E using SAXS concluded that WT mammalian Arr1 at up to 177 μM concentration was limited to dimer (33). Additionally, although Arr1 from mouse and human have been reported to form tetramers at physiological concentrations, these conclusions are based on projections of fittings of the concentration-dependent increase in molecular weight determined by MALS, where at the highest concentrations examined, the MALS signal did not reach that expected for dimers, making the conclusions speculative. One issue that limits a coherent view of mammalian Arr1 oligomerization is that previous reports do

not consistently identify which species of Arr1 were examined. While controversy remains regarding mammalian oligomerization, our results examining bArr1 agree with a monomer-dimer-tetramer model that includes the cooperative tetramer formation reported previously (12, 16).

Features of predicted xArr1 dimer structures and their physiological impact

Given the extensive similarity in the secondary and tertiary structures of xArr1 and bArr1 and the conservation of sequence within key domains, it is somewhat surprising that xArr1 did not form tetramers at the higher concentrations examined in this study. Analysis of the two predicted xArr1 dimer structures suggests that several differences between xArr1 and bArr1 dimers may explain the lack of tetramer formation. First, the crystal-predicted xArr1 CC dimer shows an interdomain rotation that appears to prevent simultaneous NN binding among a pair of CC dimers. Additionally, the apparent competition between CC, NC, and potentially other xArr1 dimer forms may sterically inhibit tetramer formation.

It is interesting to speculate why, evolutionarily, xArr1 is limited to forming dimers. One possibility is that this limitation accommodates the vastly different geometries of amphibian and mammalian rod outer segments. Amphibian rod outer segments are 6 to 8 μm in diameter and up to 60 μm long, whereas mammalian rod outer segments are significantly smaller, with diameter of ∼1 μm and length of ∼20 μm. Despite these differences in envelope geometry, the disc membrane thickness and the interdiscal spacing are identical. This leads to vastly different outer segment diffusional space that the Arr1 species need to sample to quench light activated rhodopsin and to overcome during light-dependent redistribution between the outer segment and cell body. For example, the square of the diameter ratios between amphibian and mammalian rods shows that the radial area of the interdiscal space is ∼25-64-fold larger for the amphibian outer segment, vastly increasing the space Arr1 needs to explore to find light activated rhodopsin and increasing the tortuosity of diffusion paths for axial outer segment transport. Thus, dimer or tetramer formation in amphibian versus mammalian rods appears to "tune" the Arr1 concentration and dynamics in the outer segment to optimize response termination kinetics and axial Arr1 concentration equilibration.

The limitation of xArr1 to dimers presents another interesting paradox. A recent study showed that expression of mutant mouse Arr1 (Arr1 (F86A, F198A)), that are deficient in oligomerization, at various concentrations in Arr1 KO mice lead to rod death and retinal degeneration (47). Arr1(F86A, F198A) lacks the capacity to form tetramers and the K_D for dimer formation is ∼10-fold higher (mutant K_D = 537 μM) than that of WT Arr1 (WT K_D ∼ 37 μM (16, 23)). The expression level in these studies ranged from ∼2 to 6 mM, *i.e.*, near WT Arr1 levels to ∼ 3-fold higher than Arr1 in WT rods. Thus, in these experiments, Arr1(F86A, F198A) is likely present mostly as dimers, *e.g.*, at the higher expression levels the mutant Arr1 is expected to be 84% dimer and 16% monomer. On the surface, this might suggest that amphibian rods are resistant to the toxicity of dimer Arr1 or that xArr1 lacks toxic potential, although Samaranayake *et al.* (47) interpret their results as monomer Arr1 being the toxic species. It is interesting to note that the toxic effect in this study was only observed in rods over expressing the Arr1(F86A, F198A) mutant at 2.75 to 3 times the endogenous WT Arr1 level. When expressed at WT levels, the mutant Arr1(F86A, F198A) did not lead to retinal degeneration. A useful comparison that was overlooked in this study would be the impact of over expressing WT Arr1 to similar extent as the mutant on the Arr1 knockout background. This would rule out the possibility that the degeneration observed was not simply due to gross Arr1 overexpression.

Steric volume exclusion mediated intercompartment partitioning determines the distribution of Arr1 in dark-adapted rods

It has been known for decades that Arr1 undergoes dramatic, light-dependent redistribution in mammalian and amphibian rod photoreceptors (24, 25, 42, 65, 66). In dark adapted rods, Arr1 is enriched in the cell body and depleted from the outer segment. Bright light that activates most of the rhodopsin results in a greater than 80% shift of Arr1 localization to the outer segment, likely due to a binding sink formed by bleached or bleached and phosphorylated rhodopsin (reviewed in (67, 68)). Arr1 appears to partially move to the outer segment at a threshold light intensity that approaches photoreceptor electrical response saturation (48). The amount of Arr1 that moves to the outer segment under these conditions exceeds the level of bleached rhodopsin ∼30-fold through a mechanism that remains unsolved.

The mechanism underlying dark-adapted photoreceptor Arr1 distribution is controversial. Immunohistochemistry (25, 42–47) and serial cryosectioning with western blotting (48) show Arr1 concentration in the outer segments of dark-adapted rods to be anywhere from undetectable to tenfold lower than that in the cell body and pre-synapse. The outer segment concentration of GFP-tagged Arr1 expressed in dark-adapted amphibian rods is ∼ 10% of that in the cell body (17, 24, 25). It has been proposed, although not directly tested, that low affinity binding partners throughout the inner segment, cell body and pre-synapse are responsible for the depletion of Arr1 from the outer segments of dark-adapted rods (18–20, 49, 69, 70). This lower affinity binding is speculated to allow the competitive high affinity binding of Arr1 to bleached, phosphorylated rhodopsin to draw Arr1 into the outer segment in a timely manner. Employing a quantitative computational model to directly evaluate this idea, we show that ISBPs with relatively weak affinity for Arr1 could serve to deplete Arr1 from the outer segment only if they were present in concentrations exceeding those of rhodopsin and Arr1. This analysis shows that the weak inner segment binding sink hypothesis for depletion of Arr1 from the outer segment in darkness is highly unlikely.

On the contrary, we show that partitioning by steric volume exclusion can account for most, if not all of the inner segment/cell body enrichment of Arr1, making it the predominant determinant of Arr1 distribution in dark-adapted rods. Subcellular partitioning by steric volume exclusion is an attractive model for Arr1 distribution in darkness because it can explain the enrichment and uniform distribution of Arr1 in the cell body in the absence of adequate binding partners in this compartment. Even if Arr1 were solely present as monomer, the majority of the dark-adapted distribution is explained by steric volume exclusion mediated OS-IS partitioning. Our calculations show that Arr1 dimerization with our measured K_D of ∼ 53 μM shifts the distribution to ∼90% of that observed experimentally.

Experimental procedures

Statistical analysis

K_D values were determined from curve fitting (see oligomerization models below) and 95% confidence intervals were found using the MATLAB curve fitting toolbox. Standard errors of K_Ds found from fittings were estimated according to $SD = 95\%\ CI \div 1.96$. The significance of differences between xArr1, salArr1, and xArr1 mutant K_Ds were determined by ANOVA followed by *post hoc* application of the Tukey-Kramer procedure for pair-wise comparisons (two tailed *t* test). Other statistical methods are outlined below in the appropriate Experimental procedures section.

Expression construct development and generation of point and truncation mutations

Full length WT *Xenopus* Arr1 (dCB38) was amplified using primers that added an N-terminal SalI site and C-terminal NotI site and inserted into the multiple cloning site (MCS) of pET28a (Novagen 69864) using SalI and NotI high fidelity restriction enzymes (NEB R3138L and R3189L). The Salamander Arr1 sequence was synthesized by Genewiz with EcoRI and NotI sites at the N and C-termini respectively, and then amplified and subcloned into pET28a (Novagen 69864) using the same sites. Bovine Arr1 was amplified to include an N-terminal HindIII site and C-terminal NotI site and inserted into the MCS of pET28a using HindIII (NEB R3104L) and NotI high fidelity restriction enzymes. xArr1 Y84F was created using site-directed mutagenesis with Phusion polymerase (NEB M0530L).

Primer sequences:

xArr1: 5′ ctccgtcgacacatgagtggtgaaaagaaatcc 3′, 5′ ggatttc ttttcaccactcatgtgtcgacggag 3′,

SalArr1: 5′ ctagaaagaattcatgagcacgaagatgagc 3′, 5′ ctagtttg cggccgcctatttgtc 3′ bArr1: 5′ cgacaagcttggatgggtaaggccaataagccg 3′, 5′ gagtgcggccgctcactcatccatagccgcctc 3′, Y84F: 5′ cgtaaagacctttactTtgctcggactcag 3′, 5′ ctgagtccgagcaAagtaaaggtctttacg 3′

Protein purification

Native bovine arrestin1 was purified from bovine retinas as described in Puig *et al.* (71). Constructs expressing hexa-his-tagged *Xenopus* or salamander arrestins were expressed in Rosetta *E. coli* (Novagen, 70953). Cells were induced once they reached an A_{600} nm of 0.8 to 1.0 with 35 to 50 μM IPTG depending on the construct and shaken in a Thermo Scientific MaxQ 5000 shaker at 275 RPM overnight at 18 °C. After 20 to 24 h, the cells were harvested by centrifugation for 10 min at 4000*g* in 1 L bottles. Supernatant was poured off and bottles were set upside down to dry for 2 min. All future steps were done on ice or at 4 °C. Pellets were then resuspended in 20 to 25 ml of high salt lysis buffer (20 mM Tris, pH 8.0, 600 mM NaCl, 1 mM PMSF, 5 mM BME, Roche protease inhibitor cocktail – 1 tablet/50 ml). Bacterial resuspensions were sonicated 5 rounds of 30s on ice. Sonicated resuspensions were then spun down 2 × 30 min at 16,000*g* in 50 ml conical tubes, transferring the supernatant to fresh tubes between spins. The supernatant from the second spin was incubated with 1 ml of Ni-NTA agarose per liter of culture, rotating slowly at 4 degrees C for 1 h. The slurry was then put into a gravity column and a sample of the FT was collected for gel analysis. The Ni-NTA agarose was washed with 150 ml column wash buffer per liter of cells (CWB, 20 mM Tris-Cl pH 8.0, 600 mM NaCl, 10% glycerol) + 5 mM imidazole. Then washed with 150 ml CWB + 10 mM imidazole, 150 ml CWB + 15 mM imidazole, 150 ml CWB + 20 mM imidazole. The Ni-NTA agarose was then washed with 4 × 1 ml of pre off the column and three 1 ml washes with elution buffer (20 mM Tris-Cl pH 8.0, 150 mM NaCl, scission protease buffer (50 mM Tris-Cl pH7.5, 150 mM NaCl, 1 mM EDTA, 5 mM BME) and 100 to 150 units of GST tagged prescission protease (made by our lab) was added to the column, cycled through twice, and allowed to cleave for at least 16 h. Cleaved arrestins were eluted directly with 5 mM BME and were collected from the column and pooled together with the first elution. The total sample was incubated with 200 μl glutathione-agarose shaking slowly for 1 h at 4 °C. The slurry was put on a gravity column and the flow-through collected and placed in a cassette in 2 L dialysis buffer (95 mM KCl, 15 mM NaCl, 10 mM $MgCl_2$, 10 mM Hepes, 1 mM DTT), buffer was swapped after 4 h and allowed to dialyze overnight. The dialyzed protein was then further purified over a heparin column (GE healthcare) and eluted with a 1 M salt gradient. Fractions were collected and run on a gel to select for highest purity, then pooled and put over a HiLoad 16/600 Superdex S75 pg column (GE healthcare) for gel filtration to remove any aggregates before AUC, and to exchange into an experimental buffer used previously to characterize arrestin self-association (22), which consisted of 50 mM Mops, 100 mM NaCl, pH 7.2.

Concentrations were calculated by dividing $A_{280\ nm}$ readings using the predicted extinction coefficient of the protein. Predicted extinction coefficients and molecular weights for individual proteins were obtained by inputting the exact amino acid sequences into the Expasy Protparam tool.

Analytical ultracentrifugation

Purified recombinant or endogenous Arr1 was pipetted into charcoal-filled Epon centerpieces with two sectors and

sapphire windows. All experiments were done using a Beckman Coulter ProteomLab XL-A analytical ultracentrifuge equipped with absorbance optics and a 4-hole An-60 Ti rotor at 60,000 rpm. The AUC was pre-equilibrated for at least 2 h at 10 degrees C prior to each run. Scan intervals between samples were set to zero for 200 to 300 scans and analyzed using the c(s) continuous distribution method in SEDFIT (31). Signal weight averaged sedimentation coefficients (Sw) were computed over the range of 2 to 3.5 S (amphibian) or 2 to 5.5 S (bovine) in GUSSI (72). Individual Sw values were plotted as a function of protein concentration and fitted with either a monomer-dimer (MD) or a monomer-dimer-tetramer model in MATLAB (see Binding models) to determine the Svedberg values for the monomers and each binding complex as well as the dissociation constants for the binding interactions. Symbols in Sw vs concentration plots represent individual values from single AUC runs. Some xArr1 mutations led to low expression or were unstable, limiting the concentration range and total number of concentrations possible for analysis.

xArr1 crystallization

Purified xArr1 at ∼16 mg/ml was thawed and diluted to achieve a final protein concentration of 5.3 mg/ml xArr1 in a buffer consisting of 16.5 mM MOPS–NaOH, 9 mM Tris–HCl, and 250 mM NaCl, pH 7.5. Crystallization of xArr1 was carried out by vapor diffusion in sitting-drop 96-well plates by mixing equal volumes of protein sample and crystallization buffer.

$xArr1_{SG1}$ was obtained with a crystallization buffer consisting of 140 mM ammonium chloride, 70 mM Hepes–NaOH pH 7.5, 17.5% (v/v) glycerol ethoxylate, and 6% (v/v) glycerol. Crystallization plates were initially incubated at 19 °C for 3 days and then transferred to 4 °C. Crystals with a length of 10 to 30 μm in the longest dimension were observed after 1 to 2 days. Mature crystals were harvested in MicroMeshes (MiTeGen) and flash cooled in liquid nitrogen. $xArr1_{SG2}$ was obtained with a crystallization buffer consisting of 25% (v/v) triethylene glycol, 100 mM glycine, and 100 mM ammonium sulfate (condition F2 of JBScreen Membrane, Jena Biosciences). After mixing equal volumes of protein sample and crystallization buffer, the resulting pH was 7.5. The plates were incubated at 19 °C for 7 days and then transferred to 4 °C. Crystals with a length of ∼100 μm in the longest dimension were observed after 2 weeks. Mature crystals were harvested in MicroLoops (MiTeGen) and flash cooled in liquid nitrogen.

Crystallography methods

X-ray diffraction data on the xArr1 crystals were collected at the Northeastern Collaborative Access Team (NE-CAT) beamlines at the Advanced Photon Source (APS). The intensity data were processed and merged using XDS and XSCALE (73, 74). Data from four isomorphous crystals were merged to obtain a ∼2.5 Å-resolution data set for $xArr1_{SG1}$ whereas the ∼2.9 Å-resolution data set obtained for $xArr1_{SG2}$ was collected from a single crystal. Scaled intensities were converted to amplitudes using XDSCONV (73). Data collection statistics for the two different crystal forms are shown in Table 2. Structure solution was carried out by molecular replacement using MRBUMP (75) within the CCP4 online webserver (76). An AlphaFold model of *X. laevis* arrestin-1 was used as the search model for molecular replacement. A clear solution was obtained in space group $P3_121$ with a single arrestin-1 molecule in the asymmetric unit. The initial solution was then subjected to iterative cycles of model updating and real space refinement in Coot (77) followed by reciprocal space refinement in REFMAC5 (78). The geometrical quality of model was accessed at the end of each refinement iteration using the MOLPROBITY webserver (79). In the final stages of refinement, the model was further validated using the wwPDB validation server (80). The refined $xArr1_{SG1}$ model was then used as a molecular replacement search model in Phaser (81) to solve the second xArr1 crystal form exhibiting a (= b) unit cell constants comparable to the first crystal form but with a ∼20 Å shorter c-axis. This second crystal form was solved in space group $P3_221$ with a single arrestin-1 monomer in the asymmetric unit.

Small angle Xray scattering

SAXS was performed at the Macromolecular Diffraction at Cornell High Energy Synchrotron Source (MacCHESS) G1 Station. Beam conditions were as follows: E = 9.8833 keV; beam diameter 250 μm × 250 μm; Flux = 5.9 x 10^{11} photons/s. Purified recombinant xArr1 in 50 mM Mops, 100 mM NaCl, pH 7.2, was diluted to 0.25, 0.5, 1, 1.5, 2, 2.5, 3, 3.5, 4.5, 6, and 7.6 mg/ml. Samples and buffer only were loaded in quadruplicate into the sample robot. Samples were sequentially injected onto a size exclusion column, Superdex 75 (Cytiva), the effluent of which fed directly into the X-ray beam path sample chamber, followed by a UV spectrometer. SAXS data were analyzed using the ATSAS software suite (41).

Protein painting of recombinant xArr1 protein

Recombinant xArr1 protein (20 μg) was subjected to the protein painting protocol adapted from Luchini, Espina, Liotta (82) using the molecular paint disodium; 1-amino-9,10-dioxo-4-[3-(2-sulphonatooxyethylsulphonyl) anilino] anthracene-2–sulphonate (RBB). RBB dye was resuspended in PBS (137 mm NaCl, 2.7 mM KCl, 10 mM Na2HPO4, KH2PO4, pH 7.5), and recombinant xArr1 was desalted in PBS prior to painting. The dye was added in a 1000-fold molar excess to xArr1 and incubated for 5 min at room temperature in parallel with an unpainted control sample without dye (total volume 50 uL). Unbound dye was removed by passing the reaction mixture through a Zeba 7 MW cutoff desalting column (Thermofisher) pre-equilibrated with PBS. Fractions containing xArr1 were pooled, and the protein was denatured with 2 M urea at 37 °C for 15 min. Following denaturation, the protein was

reduced with TCEP (final concentration 10 mM) for 15 min at 37 °C and alkylated with iodoacetamide (final concentration 50 mM) at room temperature in the dark for 15 min. Protein digestion was performed with mass spectrometry-grade trypsin Lys-C (Promega) at a 1:10 enzyme-to-protein ratio for 2 h at 37 °C. The reaction was stopped by the addition of glacial acetic acid and peptides were dried done. The resulting peptides were desalted using C18 column (Nest group) and dried down. Samples were dissolved in 30 µl of water containing 2% ACN and 0.5% formic acid. Two microliters (~0.5 µg) were injected onto a pulled tip nano-LC column held at to 50°C, with 75 µm inner diameter packed to 33 cm with 2.4 µm, 120 Å, C18AQ particles. The peptides were separated using a 120 min gradient from 3 to 28% ACN, followed by a 7 min ramp to 85% ACN and a 3 min hold at 85% ACN. The column was connected inline with an Orbitrap Lumos via a nanoelectrospray source operating at 2.3 kV. The mass spectrometer was operated in data-dependent top speed mode with a cycle time of 2.5s. MS^1 scans were collected at 120,000 resolution with a maximum injection time of 50 ms. Dynamic exclusion was applied for 15 s. HCD fragmentation with 35% collision energy was used followed by MS^2 scans in the ion trap a maximum 35 ms injection time. The MS data was searched using SequestHT in Proteome Discoverer (version 2.4, Thermo Scientific) simultaneously against three databases: a list of common laboratory contaminant proteins (Thermo scientific, 298 entries, 2015), Ecoli (Uniprot), and *Xenopus* (Uniprot). Enzyme specificity for trypsin was set to semi-tryptic with up to four missed cleavages. Precursor and product ion mass tolerances were 10 ppm and 0.6 Da, respectively. Cysteine carbamidomethylation was set as a fixed modification. Methionine oxidation and protein N-terminal acetylation were set as variable modifications. The output was filtered using the Percolator algorithm with strict FDR set to 0.01.

Binding models

Monomer-dimer model

The equilibrium dimerization reaction is

$$M + M \leftrightharpoons D \tag{1}$$

The equilibrium dissociation constant is

$$K_D = \frac{M^2}{D} \tag{2}$$

The total concentration of molecules is

$$C_0 = M + 2D \tag{3}$$

and thus,

$$M = C_0 - 2D \tag{4}$$

Substitution and rearrangement yields,

$$C_0{}^2 - (4C_0 + K_D)D + 4D^2 = 0 \tag{5}$$

Monomer and dimer concentrations as a function of total concentration may thus be found by solving for the negative roots of Equation 5 and substituting into Equation 4.

To fit experimentally obtained S_w versus concentration, the model-computed M and D concentrations were transformed into weighted S values according to,

$$S_w = MS_m + 2\left(\frac{M^2 S_d}{K_D C_0}\right) \tag{6}$$

where S_m and S_d are the Svedberg coefficients for monomer and dimer Arr1, respectively.

The solution of Equations 4–6 was fitted to weighted c(s) versus concentration data in MATLAB using the fit function, from which 95% confidence intervals and standard deviations of the fit parameters were calculated.

Monomer-dimer-tetramer model

The monomer-dimer-tetramer reaction is

$$4M \leftrightharpoons 2D \leftrightharpoons T \tag{7}$$

The equilibrium dissociation constants for *M-D* and *D-T* are

$$K_D^D = \frac{M^2}{D} \tag{8}$$

$$K_D^T = \frac{D^2}{T} \tag{9}$$

The total concentration of molecules is

$$C_0 = M + 2D + 4T \tag{10}$$

Substitution and rearrangement of Equations 8–10 yields,

$$4M^4 + 2K_D^D K_D^T M^2 + \left(K_D^D\right)^2 K_D^T M - C_0\left(K_D^D\right)^2 K_D^T = 0 \tag{11}$$

The concentration of monomeric Arr1 was solved by finding the real, positive roots of Equation 11, and dimer and tetramer concentrations were found from Equations 8 and 9. Values for M, D, and T were transformed to weighted S, S_w, as described in the monomer-dimer model. The solution of Equations 8–11 was fitted to weighted c(s) versus concentration in MATLAB using the fit function.

Diffusion-binding model

To evaluate the impact of local binding on the distribution of Arr1 in photoreceptors, we adopted a computational model of diffusion and local binding in one spatial dimension that we have previously published (54). In this model, the cross-

sectional area, diffusivity, and binding strength to an immobile partner could be arbitrarily varied along the spatial dimension and in time. The diffusion equation in one spatial dimension may be written as

$$\frac{\partial c}{\partial t} = D_{ap}\frac{\partial^2 c}{\partial z^2} \tag{12}$$

where D_{ap} is the apparent axial diffusion coefficient within the cell (denoted as D form here on) and z refers to the distance along the photoreceptor axis. The area of cross section (A) of rod cells and the local diffusivity of molecules varies as a function of axial position. Here, $A(z)$ refers to variation in the cross sectional area available to flux of the diffusing molecules as stated in Fick's first law of diffusion (see ref. (83)), thus, capturing 3D photoreceptor geometry in 1 spatial dimension computational space. Under these conditions the diffusion equation becomes (83),

$$\frac{\partial c(z,t)}{\partial t} = \frac{1}{A(z)}\frac{\partial\left[A(z)D(z)\frac{\partial c}{\partial z}\right]}{\partial z} \tag{13}$$

In the case of diffusion with binding we may write the modified diffusion equation (*cf.* Eq. 14.2, Crank (84)),

$$\frac{\partial c_f}{\partial t} = D_{ap}\frac{\partial^2 c}{\partial x^2} - \frac{\partial c_b}{\partial t} \tag{14}$$

where c_f is the concentration of free, diffusing molecules, c_b is the concentration of bound, non-diffusing molecules. Equation 13 thus becomes,

$$\frac{\partial c_f}{\partial t} + \frac{\partial c_b}{\partial t} = \frac{1}{A(z)}\frac{\partial}{\partial z}\left(A(z)D(z)\frac{\partial c_f}{\partial z}\right) \tag{15}$$

Assuming that binding/unbinding is much faster than diffusion, as appears to be the case with weak Arr1 self-association and Arr1–tubulin interactions, the bound concentration may be treated as an algebraic function of the free concentration,

$$c_b = f(c_f) \tag{16}$$

Substituting Equation 16 for c_b in Equation 15,

$$\frac{\partial c_f}{\partial t} = \frac{1}{\left[1 + \frac{df(c_f)}{dc_f}\right]}\frac{1}{A(z)}\frac{\partial}{\partial z}\left(A(z)D(z)\frac{\partial c_f}{\partial z}\right) \tag{17}$$

Equation 17 represents a general result for a variable area of cross section, variable diffusivity, variable binding, diffusion and binding system. Together, Equations 16 and 17 are a partial differential algebraic equation system.

Next consider binding described by a Langmuir isotherm,

$$f(c_f) = \frac{B \cdot c_f}{K_D + c_f} \tag{18}$$

where $K_D = k_{-1}/k_1$ and B is binding capacity (number of binding sites). Then,

$$\frac{df(c_f)}{dc_f} = \frac{B \cdot K_D}{(K_D + c_f)^2} = R \tag{19}$$

where R represents the binding reaction. Substitution of Equation 19 into Equation 17 yields,

$$\frac{\partial c_f}{\partial t} = \frac{1}{\left[1 + \frac{B(z)\bullet K_D(z)}{(K_D(z)+c_f)^2}\right]}\frac{1}{A(z)}\frac{\partial}{\partial z}\left(A(z)D(z)\frac{\partial c_f}{\partial z}\right)$$

$$= \frac{1}{[1 + R(z)]}\frac{1}{A(z)}\frac{\partial}{\partial z}\left(A(z)D(z)\frac{\partial c_f}{\partial z}\right) \tag{20}$$

Note that in the case of invariant D(z), Equation 20 becomes,

$$\frac{\partial c_f}{\partial t} = \frac{D}{[1 + R(z)]}\frac{1}{A(z)}\frac{\partial}{\partial z}\left(A(z)\frac{\partial c_f}{\partial z}\right) \tag{21}$$

Boundary and initial conditions

The system of Equations 16 and 20 were solved using the numerical method of lines (85, 86) where the following boundary and initial conditions were applied:

$$\frac{\partial c_f(z=0,t)}{\partial z} = \frac{\partial c_f(z=L,t)}{\partial z} = 0 \tag{22}$$

$$c_f(z,0) = c_0(z) \tag{23}$$

Equation 22 specifies no flux boundaries (homogeneous Neumann boundary conditions) at the pre-synapse (z=0) and the ciliary OS tip (z = L). Equation 23 specifies the initial distribution of molecules throughout the rod cell. The method of line is an established general algorithm for hyperbolic-parabolic (convection-diffusion equations first order in t) PDEs in which the spatial (boundary value) independent variables are replaced with algebraic approximations. The resulting system of initial value ordinary differential equations (ODEs) is then solved numerically with a library ODE integrator. In the present case, the ODE integrator is ode15s from the MATLAB library. Equations 20–23 comprise the diffusion and binding model that allows evaluation of the impact of

spatially variable diffusion and binding on dynamic transport and steady-state distributions of proteins along the length of the photoreceptor.

Data availability

The crystal structures and their associated diffraction data used in this study are available in the Protein Data Bank (PDB) under accession codes 8FUT (for $xArr1_{SG1}$) and 8FUU (for $xArr1_{SG2}$). MS data were deposited in JPOST (87), accession number JPST003382.

Supporting information—This article contains supporting information.

Acknowledgments—We thank Dr Barry Knox for providing the xArr1 expression vectors and Dr Vsevolod Gurevich for providing a vector encoding bovine Arr1 and the atomic coordinates for the bovine Arr1 solution structure model. We thank Ebbing De Jong Ebbing at the SUNY-Upstate proteomics facility for their help with mass spectrometry. We are grateful to the members of the SUNY Upstate Center for Vision Research and Department of Biochemistry and Molecular Biology for helpful discussions.

Author contributions—C. L. B., D. S., P. D. K., and P. D. C. writing–original draft; C. L. B., D. S., M. S. C., P. D. K., and P. D. C. visualization; C. L. B., D. S., M. S. C., P. D. K., and P. D. C. investigation; C. L. B., D. S., K. E. W. N., B. A. K., M. S. C., P. D. K., and P. D. C. formal analysis; C. L. B., D. S., P. D. K., and P. D. C. data curation; D. S., M. S. C., P. D. K., and P. D. C. validation; W. C. S., B. A. K., M. S. C., P. D. K., and P. D. C. writing–review and editing; W. C. S., B. A. K., and P. D. C. resources; P. D. K. and P. D. C. methodology; P. D. K. and P. D. C. funding acquisition; P. D. C. supervision; P. D. C. software; P. D. C. project administration; P. D. C. conceptualization.

Funding and additional information—This work was supported by NIH grants R01-EY018421 and R01-EY028303 (P. D. C.), R01-CA140522 (M. C.), R01-GM141033 and S10-OD023617 (B. A. K), R01-EY034519 (P. D. K.), R01-EY035768 (W. C. S.) and Department of Veterans Affairs grants I01BX004949 and I06BX006800 (P. D. K.). P. D. C. is the recipient of a Stein Innovation Award from Research to Prevent Blindness, Inc. The Department of Ophthalmology and Visual Sciences at SUNY Upstate Medical University and the Department of Ophthalmology at UC Irvine acknowledge support from unrestricted grants from Research to Prevent Blindness, Inc. We are grateful for support from New York Lions District 20Y. Portions of this work are based upon research conducted at the NE-CAT beamlines, which are funded by the National Institutes of Health (P30 GM124165). This research used resources of the APS, a U.S. DOE Office of Science User Facility operated by Argonne National Laboratory under Contract No. DE-AC02-06CH11357. Additionally, this work is based on research conducted at the Center for High-Energy X-ray Sciences (CHEXS), which is supported by the National Science Foundation (BIO, ENG and MPS Directorates) under award DMR-1829070, and the Macromolecular Diffraction at CHESS (MacCHESS) facility, which is supported by award 1-P30-GM124166-01A1 from the National Institute of General Medical Sciences, National Institutes of Health and by New York State's Empire State Development Corporation (NYSTAR).The content is solely the responsibility of the authors and does not necessarily represent the official views of any particular funding agency.

Conflicts of interest—The authors declare that they have no conflicts of interests with the contents of this article.

Abbreviations—The abbreviations used are: DEER, double electron-electron resonance spectroscopy; GPCR, G protein coupled receptor; MALS, multi-angle light scattering; ODE, ordinary differential equation; SAXS, small angle X-ray scattering.

References

1. Gurevich, V. V., and Gurevich, E. V. (2006) The structural basis of arrestin-mediated regulation of G-protein-coupled receptors. *Pharmacol. Ther.* **110**, 465–502
2. Wilden, U., Hall, S. W., and Kuhn, H. (1986) Phosphodiesterase activation by photoexcited rhodopsin is quenched when rhodopsin is phosphorylated and binds the intrinsic 48-kDa protein of rod outer segments. *Proc. Natl. Acad. Sci. U. S. A.* **83**, 1174–1178
3. Palczewski, K., Rispoli, G., and Detwiler, P. B. (1992) The influence of arrestin (48K protein) and rhodopsin kinase on visual transduction. *Neuron* **8**, 117–126
4. Dolph, P. J., Ranganathan, R., Colley, N. J., Hardy, R. W., Socolich, M., and Zuker, C. S. (1993) Arrestin function in inactivation of G protein-coupled receptor rhodopsin in vivo. *Science* **260**, 1910–1916
5. Xu, J., Dodd, R. L., Makino, C. L., Simon, M. I., Baylor, D. A., and Chen, J. (1997) Prolonged photoresponses in transgenic mouse rods lacking arrestin. *Nature* **389**, 505–509
6. Sutton, R. B., Vishnivetskiy, S. A., Robert, J., Hanson, S. M., Raman, D., Knox, B. E., *et al.* (2005) Crystal structure of cone arrestin at 2.3A: evolution of receptor specificity. *J. Mol. Biol.* **354**, 1069–1080
7. Nikonov, S. S., Brown, B. M., Davis, J. A., Zuniga, F. I., Bragin, A., Pugh, E. N., Jr., *et al.* (2008) Mouse cones require an arrestin for normal inactivation of phototransduction. *Neuron* **59**, 462–474
8. Hanson, S. M., Vishnivetskiy, S. A., Hubbell, W. L., and Gurevich, V. V. (2008) Opposing effects of inositol hexakisphosphate on rod arrestin and arrestin2 self-association. *Biochemistry* **47**, 1070–1075
9. Wacker, W. B., Donoso, L. A., Kalsow, C. M., Yankeelov, J. A., Jr., and Organisciak, D. T. (1977) Experimental allergic uveitis. Isolation, characterization, and localization of a soluble uveitopathogenic antigen from bovine retina. *J. Immunol.* **119**, 1949–1958
10. Schubert, C., Hirsch, J. A., Gurevich, V. V., Engelman, D. M., Sigler, P. B., and Fleming, K. G. (1999) Visual arrestin activity may be regulated by self-association. *J. Biol. Chem.* **274**, 21186–21190
11. Shilton, B. H., McDowell, J. H., Smith, W. C., and Hargrave, P. A. (2002) The solution structure and activation of visual arrestin studied by small-angle X-ray scattering. *Eur. J. Biochem.* **269**, 3801–3809
12. Imamoto, Y., Tamura, C., Kamikubo, H., and Kataoka, M. (2003) Concentration-dependent tetramerization of bovine visual arrestin. *Biophys. J.* **85**, 1186–1195
13. Storez, H., Scott, M. G., Issafras, H., Burtey, A., Benmerah, A., Muntaner, O., *et al.* (2005) Homo- and hetero-oligomerization of beta-arrestins in living cells. *J. Biol. Chem.* **280**, 40210–40215
14. Chen, Q., Perry, N. A., Vishnivetskiy, S. A., Berndt, S., Gilbert, N. C., Zhuo, Y., *et al.* (2017) Structural basis of arrestin-3 activation and signaling. *Nat. Commun.* **8**, 1427
15. Hanson, S. M., Gurevich, E. V., Vishnivetskiy, S. A., Ahmed, M. R., Song, X., and Gurevich, V. V. (2007) Each rhodopsin molecule binds its own arrestin. *Proc. Natl. Acad. Sci. U. S. A.* **104**, 3125–3128
16. Hanson, S. M., Van Eps, N., Francis, D. J., Altenbach, C., Vishnivetskiy, S. A., Arshavsky, V. Y., *et al.* (2007) Structure and function of the visual arrestin oligomer. *EMBO J.* **26**, 1726–1736
17. Najafi, M., Maza, N. A., and Calvert, P. D. (2012) Steric volume exclusion sets soluble protein concentrations in photoreceptor sensory cilia. *Proc. Natl. Acad. Sci. U. S. A.* **109**, 203–208

18. Smith, W. C., Bolch, S., Dugger, D. R., Li, J., Esquenazi, I., Arendt, A., *et al.* (2011) Interaction of arrestin with enolase1 in photoreceptors. *Invest. Ophthalmol. Vis. Sci.* **52**, 1832–1840
19. Nair, K. S., Hanson, S. M., Mendez, A., Gurevich, E. V., Kennedy, M. J., Shestopalov, V. I., *et al.* (2005) Light-dependent redistribution of arrestin in vertebrate rods is an energy-independent process governed by protein-protein interactions. *Neuron* **46**, 555–567
20. Huang, S. P., Brown, B. M., and Craft, C. M. (2010) Visual Arrestin 1 acts as a modulator for N-ethylmaleimide-sensitive factor in the photoreceptor synapse. *J. Neurosci.* **30**, 9381–9391
21. Chen, Q., Zhuo, Y., Kim, M., Hanson, S. M., Francis, D. J., Vishnivetskiy, S. A., *et al.* (2014) Self-association of arrestin family members. *Handb. Exp. Pharmacol.* **219**, 205–223
22. Kim, M., Hanson, S. M., Vishnivetskiy, S. A., Song, X., Cleghorn, W. M., Hubbell, W. L., *et al.* (2011) Robust self-association is a common feature of mammalian visual arrestin-1. *Biochemistry* **50**, 2235–2242
23. Hanson, S. M., Dawson, E. S., Francis, D. J., Van Eps, N., Klug, C. S., Hubbell, W. L., *et al.* (2008) A model for the solution structure of the rod arrestin tetramer. *Structure* **16**, 924–934
24. Peet, J. A., Bragin, A., Calvert, P. D., Nikonov, S. S., Mani, S., Zhao, X., *et al.* (2004) Quantification of the cytoplasmic spaces of living cells with EGFP reveals arrestin-EGFP to be in disequilibrium in dark adapted rod photoreceptors. *J. Cell Sci.* **117**, 3049–3059
25. Peterson, J. J., Tam, B. M., Moritz, O. L., Shelamer, C. L., Dugger, D. R., McDowell, J. H., *et al.* (2003) Arrestin migrates in photoreceptors in response to light: a study of arrestin localization using an arrestin-GFP fusion protein in transgenic frogs. *Exp. Eye Res.* **76**, 553–563
26. Hirsch, J. A., Schubert, C., Gurevich, V. V., and Sigler, P. B. (1999) The 2.8 A crystal structure of visual arrestin: a model for arrestin's regulation. *Cell* **97**, 257–269
27. Celver, J., Vishnivetskiy, S. A., Chavkin, C., and Gurevich, V. V. (2002) Conservation of the phosphate-sensitive elements in the arrestin family of proteins. *J. Biol. Chem.* **277**, 9043–9048
28. Vishnivetskiy, S. A., Lee, R. J., Zhou, X. E., Franz, A., Xu, Q., Xu, H. E., *et al.* (2017) Functional role of the three conserved cysteines in the N domain of visual arrestin-1. *J. Biol. Chem.* **292**, 12496–12502
29. Palczewski, K., Buczylko, J., Ohguro, H., Annan, R. S., Carr, S. A., Crabb, J. W., *et al.* (1994) Characterization of a truncated form of arrestin isolated from bovine rod outer segments. *Protein Sci.* **3**, 314–324
30. Granzin, J., Wilden, U., Choe, H. W., Labahn, J., Krafft, B., and Buldt, G. (1998) X-ray crystal structure of arrestin from bovine rod outer segments. *Nature* **391**, 918–921
31. Schuck, P. (2000) Size-distribution analysis of macromolecules by sedimentation velocity ultracentrifugation and lamm equation modeling. *Biophys. J.* **78**, 1606–1619
32. Schuck, P. (2013) Analytical ultracentrifugation as a tool for studying protein interactions. *Biophys. Rev.* **5**, 159–171
33. Granzin, J., Stadler, A., Cousin, A., Schlesinger, R., and Batra-Safferling, R. (2015) Structural evidence for the role of polar core residue Arg175 in arrestin activation. *Sci. Rep.* **5**, 15808
34. Vishnivetskiy, S. A., Schubert, C., Climaco, G. C., Gurevich, Y. V., Velez, M. G., and Gurevich, V. V. (2000) An additional phosphate-binding element in arrestin molecule. Implications for the mechanism of arrestin activation. *J. Biol. Chem.* **275**, 41049–41057
35. Zhan, X., Gimenez, L. E., Gurevich, V. V., and Spiller, B. W. (2011) Crystal structure of arrestin-3 reveals the basis of the difference in receptor binding between two non-visual subtypes. *J. Mol. Biol.* **406**, 467–478
36. Chen, Q., Zhuo, Y., Sharma, P., Perez, I., Francis, D. J., Chakravarthy, S., *et al.* (2021) An eight amino acid segment controls oligomerization and Preferred conformation of the two non-visual arrestins. *J. Mol. Biol.* **433**, 166790
37. Krissinel, E., and Henrick, K. (2007) Inference of macromolecular assemblies from crystalline state. *J. Mol. Biol.* **372**, 774–797
38. Jones, S., and Thornton, J. M. (1995) Protein-protein interactions: a review of protein dimer structures. *Prog. Biophys. Mol. Biol.* **63**, 31–65
39. Abramson, J., Adler, J., Dunger, J., Evans, R., Green, T., Pritzel, A., *et al.* (2024) Accurate structure prediction of biomolecular interactions with AlphaFold 3. *Nature* **630**, 493–500
40. Gurevich, V. V., Hanson, S. M., Song, X., Vishnivetskiy, S. A., and Gurevich, E. V. (2011) The functional cycle of visual arrestins in photoreceptor cells. *Prog. Retin. Eye Res.* **30**, 405–430
41. Manalastas-Cantos, K., Konarev, P. V., Hajizadeh, N. R., Kikhney, A. G., Petoukhov, M. V., Molodenskiy, D. S., *et al.* (2021) Atsas 3.0: expanded functionality and new tools for small-angle scattering data analysis. *J. Appl. Crystallogr.* **54**, 343–355
42. Philp, N. J., Chang, W., and Long, K. (1987) Light-stimulated protein movement in rod photoreceptor cells of the rat retina. *FEBS Lett.* **225**, 127–132
43. Mendez, A., Lem, J., Simon, M., and Chen, J. (2003) Light-dependent translocation of arrestin in the absence of rhodopsin phosphorylation and transducin signaling. *J. Neurosci.* **23**, 3124–3129
44. Zhang, H., Huang, W., Zhang, H., Zhu, X., Craft, C. M., Baehr, W., *et al.* (2003) Light-dependent redistribution of visual arrestins and transducin subunits in mice with defective phototransduction. *Mol. Vis.* **9**, 231–237
45. Orisme, W., Li, J., Goldmann, T., Bolch, S., Wolfrum, U., and Smith, W. C. (2010) Light-dependent translocation of arrestin in rod photoreceptors is signaled through a phospholipase C cascade and requires ATP. *Cell Signal.* **22**, 447–456
46. Grossman, G. H., Watson, R. F., Pauer, G. J., Bollinger, K., and Hagstrom, S. A. (2011) Immunocytochemical evidence of Tulp1-dependent outer segment protein transport pathways in photoreceptor cells. *Exp. Eye Res.* **93**, 658–668
47. Samaranayake, S., Vishnivetskiy, S. A., Shores, C. R., Thibeault, K. C., Kook, S., Chen, J., *et al.* (2020) Biological role of arrestin-1 oligomerization. *J. Neurosci.* **40**, 8055–8069
48. Strissel, K. J., Sokolov, M., Trieu, L. H., and Arshavsky, V. Y. (2006) Arrestin translocation is induced at a critical threshold of visual signaling and is superstoichiometric to bleached rhodopsin. *J. Neurosci.* **26**, 1146–1153
49. Nair, K. S., Hanson, S. M., Kennedy, M. J., Hurley, J. B., Gurevich, V. V., and Slepak, V. Z. (2004) Direct binding of visual arrestin to microtubules determines the differential subcellular localization of its splice variants in rod photoreceptors. *J. Biol. Chem.* **279**, 41240–41248
50. Smith, T. S., Spitzbarth, B., Li, J., Dugger, D. R., Stern-Schneider, G., Sehn, E., *et al.* (2013) Light-dependent phosphorylation of Bardet-Biedl syndrome 5 in photoreceptor cells modulates its interaction with arrestin1. *Cell Mol. Life Sci.* **70**, 4603–4616
51. Nickell, S., Park, P. S., Baumeister, W., and Palczewski, K. (2007) Three-dimensional architecture of murine rod outer segments determined by cryoelectron tomography. *J. Cell Biol.* **177**, 917–925
52. Gilliam, J. C., Chang, J. T., Sandoval, I. M., Zhang, Y., Li, T., Pittler, S. J., *et al.* (2012) Three-dimensional architecture of the rod sensory cilium and its disruption in retinal neurodegeneration. *Cell* **151**, 1029–1041
53. Corless, J. M., Fetter, R. D., Zampighi, O. B., Costello, M. J., and Wall-Buford, D. L. (1987) Structural features of the terminal loop region of frog retinal rod outer segment disk membranes: II. Organization of the terminal loop complex. *J. Comp. Neurol.* **257**, 9–23
54. Maza, N. A., Schiesser, W. E., and Calvert, P. D. (2019) An intrinsic compartmentalization code for peripheral membrane proteins in photoreceptor neurons. *J. Cell Biol.* **218**, 3753–3772
55. Hanson, S. M., Cleghorn, W. M., Francis, D. J., Vishnivetskiy, S. A., Raman, D., Song, X., *et al.* (2007) Arrestin mobilizes signaling proteins to the cytoskeleton and redirects their activity. *J. Mol. Biol.* **368**, 375–387
56. Zhuang, T., Chen, Q., Cho, M. K., Vishnivetskiy, S. A., Iverson, T. M., Gurevich, V. V., *et al.* (2013) Involvement of distinct arrestin-1 elements in binding to different functional forms of rhodopsin. *Proc. Natl. Acad. Sci. U. S. A.* **110**, 942–947
57. Song, X., Vishnivetskiy, S. A., Seo, J., Chen, J., Gurevich, E. V., and Gurevich, V. V. (2011) Arrestin-1 expression level in rods: balancing functional performance and photoreceptor health. *Neuroscience* **174**, 37–49
58. Pugh, E. N., Jr., and Lamb, T. D. (2000) Phototransduction in vertebrate rods and cones: molecular mechanisms of amplification, recovery and light adaptation. In: Stavenga, D. G., ed. *Handbook of Biological Physics*, Elsevier Science B. V.: 183–255

59. Nagle, B. W., Doenges, K. H., and Bryan, J. (1977) Assembly of tubulin from cultured cells and comparison with the neurotubulin model. *Cell* **12**, 573–586
60. Hiller, G., and Weber, K. (1978) Radioimmunoassay for tubulin: a quantitative comparison of the tubulin content of different established tissue culture cells and tissues. *Cell* **14**, 795–804
61. Nelson, T. S., Simpson, C., Dyka, F., Dinculescu, A., and Smith, W. C. (2022) A modified Arrestin1 increases Lactate production in the retina and slows retinal degeneration. *Hum. Gene Ther.* **33**, 695–707
62. Pulvermuller, A., Maretzki, D., Rudnicka-Nawrot, M., Smith, W. C., Palczewski, K., and Hofmann, K. P. (1997) Functional differences in the interaction of arrestin and its splice variant, p44, with rhodopsin. *Biochemistry* **36**, 9253–9260
63. Rosenkranz, J. (1973) New results on the ultrastructure of frog rod outer segments. *Z Zellforsch. Mikrosk. Anat.* **143**, 45–52
64. Townes-Anderson, E., MacLeish, P. R., and Raviola, E. (1985) Rod cells dissociated from mature salamander retina: ultrastructure and uptake of horseradish peroxidase. *J. Cell Biol.* **100**, 175–188
65. Broekhuyse, R. M., Tolhuizen, E. F., Janssen, A. P., and Winkens, H. J. (1985) Light induced shift and binding of S-antigen in retinal rods. *Curr. Eye Res.* **4**, 613–618
66. Mirshahi, M., Thillaye, B., Tarraf, M., de Kozak, Y., and Faure, J. P. (1994) Light-induced changes in S-antigen (arrestin) localization in retinal photoreceptors: differences between rods and cones and defective process in RCS rat retinal dystrophy. *Eur. J. Cell Biol.* **63**, 61–67
67. Calvert, P. D., Strissel, K. J., Schiesser, W. E., Pugh, E. N., Jr., and Arshavsky, V. Y. (2006) Light-driven translocation of signaling proteins in vertebrate photoreceptors. *Trends Cell Biol.* **16**, 560–568
68. Barnes, C. L., Malhotra, H., and Calvert, P. D. (2021) Compartmentalization of photoreceptor sensory cilia. *Front. Cell Dev. Biol.* **9**, 636737
69. Peterson, J. J., Orisme, W., Fellows, J., McDowell, J. H., Shelamer, C. L., Dugger, D. R., *et al.* (2005) A role for cytoskeletal elements in the light-driven translocation of proteins in rod photoreceptors. *Invest. Ophthalmol. Vis. Sci.* **46**, 3988–3998
70. Smith, W. C., Peterson, J. J., Orisme, W., and Dinculescu, A. (2006) Arrestin translocation in rod photoreceptors. *Adv. Exp. Med. Biol.* **572**, 455–464
71. Puig, J., Arendt, A., Tomson, F. L., Abdulaeva, G., Miller, R., Hargrave, P. A., *et al.* (1995) Synthetic phosphopeptide from rhodopsin sequence induces retinal arrestin binding to photoactivated unphosphorylated rhodopsin. *FEBS Lett.* **362**, 185–188
72. Brautigam, C. A. (2015) Calculations and publication-quality illustrations for analytical ultracentrifugation data. *Methods Enzymol.* **562**, 109–133
73. Kabsch, W. (2010) Xds. *Acta Crystallogr. D* **66**, 125–132
74. Kabsch, W. (2010) Integration, scaling, space-group assignment and post-refinement. *Acta Crystallogr. D* **66**, 133–144
75. Keegan, R. M., and Winn, M. D. (2008) MrBUMP: an automated pipeline for molecular replacement. *Acta Crystallogr. D* **64**, 119–124
76. Winn, M. D., Ballard, C. C., Cowtan, K. D., Dodson, E. J., Emsley, P., Evans, P. R., *et al.* (2011) Overview of the CCP4 suite and current developments. *Acta Crystallogr. D* **67**, 235–242
77. Emsley, P., Lohkamp, B., Scott, W. G., and Cowtan, K. (2010) Features and development of Coot. *Acta Crystallogr. D* **66**, 486–501
78. Murshudov, G. N., Skubak, P., Lebedev, A. A., Pannu, N. S., Steiner, R. A., Nicholls, R. A., *et al.* (2011) REFMAC5 for the refinement of macromolecular crystal structures. *Acta Crystallogr. D* **67**, 355–367
79. Williams, C. J., Headd, J. J., Moriarty, N. W., Prisant, M. G., Videau, L. L., Deis, L. N., *et al.* (2018) MolProbity: more and better reference data for improved all-atom structure validation. *Protein Sci.* **27**, 293–315
80. Read, R. J., Adams, P. D., Arendall, W. B., 3rd, Brunger, A. T., Emsley, P., Joosten, R. P., *et al.* (2011) A new generation of crystallographic validation tools for the protein data bank. *Structure* **19**, 1395–1412
81. McCoy, A. J., Grosse-Kunstleve, R. W., Adams, P. D., Winn, M. D., Storoni, L. C., and Read, R. J. (2007) Phaser crystallographic software. *J. Appl. Crystallogr.* **40**, 658–674
82. Luchini, A., Espina, V., and Liotta, L. A. (2014) Protein painting reveals solvent-excluded drug targets hidden within native protein-protein interfaces. *Nat. Commun.* **5**, 4413
83. Calvert, P. D., Schiesser, W. E., and Pugh, E. N., Jr. (2010) Diffusion of a soluble protein, photoactivatable GFP, through a sensory cilium. *J. Gen. Physiol.* **135**, 173–196
84. Crank, J. (1975) *The Mathematics of Diffusion*, 2nd Ed., Oxford University Press, Oxford
85. Schiesser, W. E. (1991) *The Numerical Method of Lines: Integration of Partial Differential Equations*, Academic Press, New York
86. Schiesser, W. E., and Griffiths, G. W. (2009) *A Compendium of Partial Differential Equation Models: Method of Lines Analysis with MATLAB*, Cambridge University Press, New York
87. Okuda, S., Watanabe, Y., Moriya, Y., Kawano, S., Yamamoto, T., Matsumoto, M., *et al.* (2017) jPOSTrepo: an international standard data repository for proteomes. *Nucleic Acids Res* **45**, D1107–D1111
88. Sievers, F., Wilm, A., Dineen, D., Gibson, T. J., Karplus, K., Li, W., *et al.* (2011) Fast, scalable generation of high-quality protein multiple sequence alignments using Clustal Omega. *Mol. Syst. Biol.* **7**, 539
89. Gouet, P., Robert, X., and Courcelle, E. (2003) ESPript/ENDscript: Extracting and rendering sequence and 3D information from atomic structures of proteins. *Nucleic Acids Res.* **31**, 3320–3323